A PRELIMINARY EVALUATION OF ADVANCED DVORAK TECHNIQUE-DERIVED INTENSITY ESTIMATE ERRORS AND BIASES DURING THE EXTRATROPICAL TRANSITION OF TROPICAL CYCLONES USING SYNTHETIC SATELLITE IMAGERY

by

Alexander Manion

A Thesis Submitted in

Partial Fulfillment of the

Requirements for the Degree of

Masters of Science

in Mathematics

at

The University of Wisconsin-Milwaukee

August 2014

ABSTRACT
A PRELIMINARY EVALUATION OF ADVANCED DVORAK TECHNIQUE-DERIVED INTENSITY ESTIMATE ERRORS AND BIASES DURING THE EXTRATROPICAL TRANSITION OF TROPICAL CYCLONES USING SYNTHETIC SATELLITE IMAGERY

by

Alexander Manion

The University of Wisconsin-Milwaukee, 2014
Under the Supervision of Professor Clark Evans

Real-time and historical tropical cyclone (TC) intensity estimates during extratropical transition (ET) are derived mainly from satellite-based methods such as the Dvorak Technique (DT) and Advanced Dvorak Technique (ADT). However, the empirical relationships developed between cloud organization patterns and cyclone intensity that underlie the DT and ADT are primarily tropical in nature and thus become less reliable during ET. Preliminary analyses suggest that ADT-derived intensity estimates are weak-biased during ET; however, due to the lack of direct observations of cyclone intensity during ET, the extent to which this is true is unknown. Herein, an attempt to quantify errors during this process is evaluated. Synthetic satellite imagery obtained from numerical simulations of five representative North Atlantic ET events between 1990 – 2013, spanning five microphysics schemes, are used to quantify ADT-derived intensity estimate errors during ET. Model-derived hourly time series of minimum sea level pressure and maximum sustained surface wind speed obtained from each simulation serve as a proxy for "observed" TC intensity to which ADT-derived intensity estimates are

compared. Results suggest that ADT-derived composite intensity estimates are weak-biased, with mean errors that are largest during the onset of ET and become somewhat smaller as ET ends. An alternative means of obtaining intensity estimates during ET, utilizing an empirical orthogonal function-based linear regression model, is developed and evaluated. The linear regression model shows promise in providing improved intensity estimates during ET; however, the small sample size of cases used in its development precludes any meaningful conclusions from being derived from the analysis.

TABLE OF CONTENTS

LIST OF FIGURES

lines indicate the 500-km radius. (right) Height difference (ΔZ) within this radius. Cyclone phase is derived from thermal wind [$\partial(\Delta Z)/\partial \ln p$] in two layers. $-V_L^T$ is calculated using a linear-regression fit of ΔZ between 900 and 600 hPa, while $-V_U^T$ is calculated similarly between 600 and 300 hPa. Anomaly from zonal mean (dotted on left) clearly illuminates cyclone tilt in (b). It is the tilt that leads to the correct cold-core diagnosis in (b). The data sources used to obtain each panel are as in Figure 5. Reproduced from Hart (2003), their Figure 3.

11. Cyclone phase space diagram, depicting lower tropospheric thermal wind ($-V_L^T$, horizontal axis) and lower tropospheric thermal asymmetry (B, vertical axis), for North Atlantic Hurricane Floyd between 1200 UTC 9 September 1999 and 1200 UTC 19 September 1999. Diagram obtained from 1° NOGAPS model operational analyses. The start (end) of the cyclone's trajectory through the phase space is depicted by an A (a Z). The relative intensity of the cyclone, as assessed utilizing minimum sea level pressure, is given by the color shading of each circle, with darker colors denoting a more intense cyclone. The relative size of the cyclone's 925 hPa gale-force (>17 m s^{-1}) wind field is given by the size of the color-shaded circle. Reproduced from Hart (2003), their Figure 6a.

12. Best track and model-derived ("truth") pressure (hPa) intensity values for (a) Edouard, (b) Erin, (c) Leslie, (d) Noel, and (e) Ophelia. Vertical left and right dashed lines represent average ET start and ET end times respectively.

13. Best track and model-derived ("truth") wind (kt) intensity values for (a) Edouard, (b) Erin, (c) Leslie, (d) Noel, (e) Ophelia. Vertical left and right dashed lines represent average ET start and ET end times respectively.

19. Model-Derived (“Truth”) minus ADT-Estimated Pressure (hPa) Error for all storms within their respective microphysical scheme, normalized to the ET timeline.

20. Model-Derived (“Truth”) minus ADT-Estimated Wind (kt) Error for all storms within their respective microphysical scheme, normalized to the ET timeline.

21. Model-Derived (“Truth”) minus ADT-Estimated Pressure (hPa) Error for similar storms with varying microphysical scheme, normalized to the ET timeline.

22. Model-Derived (“Truth”) minus ADT-Estimated Wind (kt) Error for similar storms with varying microphysical scheme, normalized to the ET timeline.

23. SSI for Edouard, taken on 09/01 18Z or 48 hours into the simulation. A visible eye is not seen at anytime in Edouard as it displays upper level clouds (denoted by cold cloud top temperatures) both over the storm center and northeast of storm center.

24. SSI for Erin on 09/13 20Z or 61 hours into the simulation. Erin displays a discernable eye leading into ET start, where it is quickly eroded by cold, descending air from the northwest of storm center (not pictured).

25. SSI for Leslie at 09/10 06Z or 72 hours into the simulation. A discernable large eye is seen leading into the start of ET.

26. SSI for Noel at 11/02 00Z or 48 hours into the simulation. An eye is not seen throughout any part of the simulation. The Thompson, Morrison, and Milbrandt cases display an excess amount of upper-level clouds to the north, south, and east of the storm.

27. SSI for Ophelia on 10/02 06Z or 66 hours into the simulation. The WSM6 case shows a discernable eye leading up to ET start, while the WDM6 and Milbrandt

LIST OF TABLES

ACKNOWLEDGMENTS

I would like to thank my advising professor, Dr. Clark Evans at UW-Milwaukee, for his contributions and guidance throughout this project.

I would like to thank Dr. Sergey Kravtsov at UW-Milwaukee for his guidance of the EOF-based linear regression model used within this report.

I would like to thank Chris Velden, Tim Olander and John Sears at the Cooperative Institute for Meteorological Satellite Studies (CIMSS) at UW-Madison for their guidance and expertise with the Advanced Dvorak Technique (ADT) and for running ADT on synthetic satellite imagery.

Lastly, I would like to thank Dr. Louie Grasso at the Cooperative Institute for Research in the Atmosphere (CIRA) at Colorado State University for his contribution in the production of synthetic satellite imagery.

I. Introduction

A tropical cyclone (TC) that transitions into an extratropical cyclone, a process known as extratropical transition (ET), has the potential to produce sustained gale-force winds, large waves, and heavy rainfall as it moves into higher latitudes. ET occurs in nearly every ocean basin that hosts TCs, with the largest number of ET events occurring in the western North Pacific and the greatest percentage (45%) of all TCs that undergo ET found in the North Atlantic basin (Jones et al. 2003). The societal impacts resulting from an ET event can be substantial. Over land, the ET of Tropical Storm Agnes (1972) led to one of the worst natural flood disasters in United States history with total damages amounting to $3.5 billion (DiMego and Bosart 1982). The ET of Tropical Storm Janis (1995) produced severe flooding and mudslides across Korea, leading to at least 45 deaths and nearly 22,000 people left homeless (JTWC 1995). More recently, Hurricane Sandy (2012), which completed ET shortly before making landfall in the northeastern United States, was responsible for at least 72 deaths and approximately $50 billion in damage across the United States (e.g., Blake et al. 2013). Over water, 75 m s^{-1} wind gusts generated by the ET of TC Gisele capsized a ferry that resulted in the loss of 51 lives (Hill 1970). Despite the high frequency of ET occurrence and societal risks and impacts associated with ET events, direct observations of storm intensity during ET are virtually non-existent. Furthermore, present remote-sensing-based methods for estimating storm intensity (e.g., the Dvorak and Advanced Dvorak techniques of Dvorak (1984) and Olander and Velden (2007), respectively) are not well-suited to assessing storm intensity during ET (Velden et al. 2006). The exponential

relationship between infrastructural damage and surface wind speed (e.g., Karl et al. 2008) makes obtaining accurate estimates of a transitioning storm's intensity of both scientific and societal importance. This is augmented by the fact that a storm's surface wind field typically expands in areal extent, even as the maximum sustained surface winds typically weaken during ET (Evans and Hart 2008), thereby expanding the area over which potentially damaging winds may be felt.

The Dvorak Technique (DT) is an empirically-derived method that uses a set of measurements and rules to subjectively estimate TC intensity from satellite cloud signatures and brightness temperatures values (Dvorak 1984). A study by Brown and Franklin (2004) found that 50% of maximum sustained (surface) winds (MSW) estimated by the DT are within 5 kt of reconnaissance aircraft measurement-aided "best track" (Jarvinen et al. 1984) estimates. However, the accuracy of any given DT-based intensity estimate is partially a function of the skill level of the forecaster applying the DT. Consequently, the Advanced Dvorak Technique (ADT; Olander and Velden 2007) was developed to help alleviate this issue. ADT is an automated method that uses primarily geostationary infrared satellite imagery to estimate tropical cyclone intensity. ADT-estimated intensity values throughout the entirety of a tropical cyclone's lifecycle (depression, storm, and hurricane) are competitive with subjectively-obtained DT intensity estimates (Olander and Velden 2007).

However, both the DT and ADT rely upon empirical relationships between cloud patterns and cyclone intensity that are primarily tropical in nature. This poses a challenge during ET, during which the interaction of a TC with an upstream trough causes the TC's cloud field to become highly asymmetric due to the erosion of deep,

moist convection upstream and equatorward of the TC's center (Klein et al. 2000). Thus, satellite-based estimates often are less reliable once a tropical storm or cyclone begins ET (Velden et al. 2006). To illustrate this, we verify ADT-derived intensity estimates for twelve near-land TCs in the North Atlantic basin between 2005 and 2008 that are within two days of completing ET against direct measurements of maximum intensity. In the composite mean, ADT-derived intensity estimates are 8.47 hPa and 13.12 kt too weak for minimum sea level pressure and maximum 10-m wind speed, respectively, compared to observations. However, only eighteen individual observations are available for verification, once again highlighting the lack of direct observations that are available during ET events. While preliminary results suggest that the ADT is weak-biased during ET, which we hypothesize to reflect the partial maintenance of the transitioning TC's intensity via the extraction of kinetic energy from the vertically-sheared synoptic-scale flow associated with the aforementioned upstream trough, the precise magnitude and temporal evolution of such a bias remains unknown.

To improve satellite-derived intensity estimates during ET, it is presumed that a new empirical relationship between cloud patterns and cyclone intensity applicable during ET must be developed. However, to do so requires extensive databases of cloud patterns (such as provided by geostationary and polar-orbiting satellites) and direct measurements of cyclone intensity during ET. While the former is available, the latter is not, barring a costly increase in the number and spatial extent of such *in situ* observations. Thus, an alternative means is necessary. As the initial step toward improving such estimates, herein we propose an alternative method for assessing

the biases associated with ADT-derived intensity estimates during ET that utilizes intensity time series and synthetic satellite imagery derived from numerical simulations of multiple ET events.

Model-derived intensity time series, serving as a proxy for "direct" observations, are obtained for five North Atlantic basin TCs that underwent ET. Synthetic satellite imagery derived utilizing a radiative transfer model applied to numerical simulation output of each ET event is used to evaluate ADT estimates during ET. Sensitivity in the synthetic-satellite-based, ADT-derived intensity estimates to the parameterized representation of cloud-scale processes is evaluated utilizing an ensemble of five microphysical-parameterization-varying simulations for each case. Error statistics, defined as model "truth" minus ADT-based "estimate", are normalized to the ET timeline of Evans and Hart (2003), thus allowing for an internally-consistent comparison between "truth" and "estimate" over all cases examined. The primary aim of this study is to obtain precise magnitudes and temporal evolutions of satellite-based intensity estimate errors and biases during ET. A concurrent aim of this study is to evaluate whether synthetic satellite imagery can be utilized not just for model evaluation (e.g., Jankov et al. 2011, Bikos et al. 2012, Grasso et al. 2014, and Jin et al. 2014) but also for applications such as the ADT, which evaluates cloud organization and, in some cases, brightness temperature values and their spatial gradients meeting or exceeding given threshold values to estimate TC intensity.

The remainder of this thesis is structured as follows. A review of the relevant literature is presented in section 2. The methodology underlying this study is

further explained in section 3. Study results are presented in section 4, with a discussion and conclusion following in sections 5 and 6 respectively.

II. Literature Review

a) Dvorak Technique

The advent of satellites enabled researchers to determine that the organization and intensity of a TC's clouds could be used to estimate its intensity. The appearance of a storm's eye, the presence of banding structures, and the size of the cloud pattern were all used in the early 1960s as a first-guess for storm intensity. However, at that time only one satellite picture a day – and that during the daytime hours – was available. By the late 1970s, however, the temporal interval between successive images had decreased substantially while infrared sensors allowed for nighttime remote sensing of clouds to begin (Dvorak 1984). The rightmost column of Table 1 displays a listing of key satellite milestones between the 1950s and 1980.

Access to multiple satellite images per day allowed scientists to empirically derive relationships between cloud patterns typically seen with TCs and the intensity associated with said patterns. For example, observations from infrared satellite showed either an increase in cold clouds surrounding the eye and/or the warming of the eye could also be used to estimate intensity values, with a larger temperature gradient between the two indicating stronger storm intensity (Velden et al. 2006). Ultimately, these observations led to the creation of the Dvorak Technique (DT), an empirical method relating satellite cloud patterns and brightness temperature values to TC intensity (Dvorak 1984).

Dvorak (1984) noted four cloud patterns (hereafter referred to as scene types) that are observed throughout the evolution of a tropical cyclone: curved band, central dense overcast (CDO), eye, and shear. Each scene type is assigned a T number (T#) throughout the tropical cyclone's lifespan, with higher T numbers corresponding to greater intensity values. The relationships between cloud organization and T# for the four aforementioned scene types are depicted in Figure 1. The first (second) row displays the curved band scene type as depicted in visible (enhanced infrared) satellite imagery. The CDO scene type, corresponding to the third row of Figure 1, is assigned when dense, overcast clouds appear over the eye or over underlying curved cloud features of the storm. An increase in the aerial extent of the overcast region and/or an increase of banding of clouds along the edge of the region both correlate to a higher T#. The shear scene type, the weakest of the patterns, is employed when moderate to strong vertical wind shear prevents the clouds from coiling around the storm center. If an eye is identified, enhanced infrared images are used and two temperature measurements are taken: one of the coldest band of clouds surrounding the eye and another within the eye itself. The larger the temperature gradient between the two, the larger the assigned T#. Subsequently, the T# is converted into a current intensity (CI) number, from which the maximum mean wind speed (MWS) and minimum sea level pressure (MSLP) are empirically derived (Table 2). The CI number is equivalent to the T# during the developing stages of a tropical cyclone and is kept higher than the T# when the cyclone weakens. In general, the T# can be thought of a good first guess intensity estimate, while the CI number is the final intensity estimate after subjective rules

and constraints upon intensity change with time have been applied (Dvorak 1984).

The DT has two primary shortcomings. First, the storm center has to be manually determined by the user. If an eye has not developed, is obscured by overlying clouds, or is too small to be observed by satellite, the user may incorrectly identify a storm's center, resulting in an erroneous T# given that most scene type-based intensity estimates are highly dependent upon the amount of curvature around the storm center location. Secondly, infrared imagery may reflect an obscured eye due to the presence of a broad area of light cirrus clouds (with cold cloud-top brightness temperatures) over the storm center. Such clouds are usually transparent, or nearly so, in visible satellite imagery. This may result in the user incorrectly determining a CDO scene type instead of an eye scene type, resulting in an underestimation of storm intensity. Consequently, a fair amount of subjectivity is inherent to each DT analysis, as user expertise can vary substantially (Velden et al. 2006).

b) Advanced Dvorak Technique

In 2004, the Advanced Dvorak Technique (ADT), a fully automated, computer-based objective scheme for estimating tropical cyclone intensity became operational. Not only is the ADT an objective application of the empirical DT that lessens subjectivity due to analyst judgment, but also it employs an automated storm centering determination processes and a variety of new rules, constraints, and scene types to produce intensity estimates that are competitive with DT estimates (Olander and Velden 2007).

The initial step in determining a storm center within ADT involves using an

interpolation of an official tropical cyclone warning center short-term track forecast as a first guess for the storm center location. Next, the ADT centering method is employed as followed: If the previous final T# intensity lies between 3.5 and 4.5 and three or more eye or embedded scene types have been previously identified, the Spiral Centering (SC) and Eye Ring Fitting (RF) methods (described below) will be used. Once the final T# value has exceeded 4.5, both auto-centering techniques will be utilized. Otherwise, the first guess center location is used as the ADT center point (Olander and Velden 2013).

The SC routine finds the maximum alignment between the cloud top temperature gradient and a 5-degree log spiral vector originating from the center region within different analysis regions (Figure 2), which are determined within a remapped rectilinear grid (Olander and Velden 2013). To further improve upon the SC-determined storm center, the RF analysis method is performed. This method uses the SC center point and searches around it for intense gradients using several small ring shaped areas (Figure 3). Finally, a confidence factor score is determined to derive which of the two techniques described above (SC or a combination of both), if any, will be used to determine the center point for the image being analyzed. If the scheme is not able to find a good spiral pattern match using the SC technique, or if the ADT determined storm center position is too far separated from the initial first guess, the first guess storm center location will be used.

In addition to the scene types used in the DT, the ADT uses two new eye scene types, large eye and pinhole eye, and one new cloud scene type, irregular CDO. Large eye is employed when the radius of the eye is equal to or larger than 38 km,

whereas pinhole eye is used when the radius of the eye is less than or equal to five km. Irregular CDO is similar to the CDO scene type described in the DT, except that the cloud region is not directly centered over the eye. Examples of ADT eye and cloud scene types can be seen in Figures 4 and 5.

The ADT utilizes a scene score to relate multiple cloud and eye parameters to TC intensity for each of the various scene types. The parameters are identified within 136 km of the storm center, with examples of such parameters including temperature of the eye, difference between cloud and eye temperatures (ΔT), cloud region size, and the T# that was recorded twelve hours previous. Next, additional checks are implemented to further refine the scene type and intensity estimates, including cloud region temperature (T_{cloud}), cloud region symmetry (sym_{cloud}), cloud region CDO radius (R_{cdo}), and eye radius (to select between the three eye scene types).

Cloud region temperature (T_{cloud}) is defined as the average cloud top temperature within an 80km-wide annulus centered on the storm center location, with colder cloud top temperatures corresponding to higher intensity estimates (Figure 6a). Cloud region symmetry (sym_{cloud}) is computed as the temperature difference between the area-averaged temperatures of opposite λ=15° wide sectors. The final sym_{cloud} value is computed by averaging all the difference values over an 80 km wide annulus centered on the storm center. Higher estimated intensities are assumed for storms that are symmetrical (Figure 6b). Eye minus cloud region temperatures (ΔT) are calculated by finding the eye region maximum temperature and subtracting that value from the cloud region average temperature (T_{cloud}), with

large temperature differences between the two parameters corresponding to higher intensity estimates (Figure 6c). The cloud region CDO radius (R_{cdo}) reflects the size of a CDO scene type as determined from the average of four radial measurements centered on storm center position, with a larger average radial measurement corresponding to more intense estimates (Figure 6d).

Intensities for all scene types, except for the curved band and shear scene types, are derived using linear regression equations. Intensity values for spiral band are found by placing a 10-degree log spiral to determine convective cloud curvature, with greater curvature corresponding to greater intensity. The shear scene type derives its intensity values by measuring the distance between the storm center position and the main convective band, with a greater distance between the two corresponding to weaker intensity values.

A final T# is assigned to the corresponding scene type, from which the CI# is derived after applying a set of rules, constraints, and corrections as described by Olander and Velden (2007). The CI# is then used to estimate storm intensity using an empirically derived relationship similar to Table 2 (e.g., Table 3 of Olander and Velden 2007).

c) Synthetic Satellite Imagery

To employ the ADT in this work, synthetic satellite imagery (SSI) derived from numerical simulation output is utilized. Most generally, a forward radiative transfer model is utilized to compute top-of-the-atmosphere brightness temperatures from numerical simulation output for selected satellite imager bands (e.g., Grasso et al. 2008, Bikos et al. 2012). Hydrometeor particle sizes used in

obtaining SSI are computed utilizing mass mixing ratios and, where available, number concentrations predicted by the microphysical parameterization utilized within a given numerical simulation. Operationally, SSI has proven useful in identifying simulated jet streaks and shortwave troughs that may spark or intensify deep convection, contributing to improved cloud cover forecasts, and in depicting simulated convection initiation events, among other applications (Bikos et al. 2012).

Other recent studies have utilized SSI as a means of model evaluation and validation, particularly as it relates to microphysical and planetary boundary layer parameterizations. Several of these studies are discussed below. Cintineo et al. (2014) evaluated the performance of planetary boundary layer and cloud microphysical parameterization schemes using synthetic GOES-13 satellite observations in 4 km horizontal grid spacing convection-permitting ensemble forecasts. Comparisons between real and synthetic GOES-13 infrared brightness temperatures showed that large differences in simulated cloud cover and brightness temperatures exist between simulations utilizing different microphysical schemes. Variability in simulated cloud cover and brightness temperatures was more subdued and localized (in time and, to some extent, altitude) between simulations utilizing different PBL schemes. The Milbrandt and Yau, and Morrison microphysical schemes produce too many clouds in the upper troposphere, resulting in colder cloud top temperatures. Conversely, the WDM6 and Thompson microphysical schemes underproduce upper-level clouds, resulting in warmer cloud top temperatures compared to observations. Spatially, the Milbrandt and Yau and Morrison schemes overforecasted the aerial extent of upper-level cloud cover by

over 50%, while the WDM6 underpredicted the extent by 40%. The Thompson scheme demonstrated the most skill, with aerial extent staying close to a 1:1 ratio with observed throughout the forecast period. Additionally, the Thompson scheme produced the most accurate brightness temperatures for values less than 240° K for the cases examined in this study despite its aforementioned underprediction of the coldest upper-level clouds.

Jankov et al. (2010) used synthetic GOES-10 satellite imagery at 10.7 μm (longwave infrared) derived from Advanced Research Weather and Forecasting (WRF-ARW) numerical model output with an outer domain consisting of 20 km horizontal grid spacing and an inner nest with 4 km horizontal grid spacing to evaluate an atmospheric river event that took place in California on December 30-31, 2005. The WSM6 and Morrison schemes best resembled the spatial cloud coverage pattern when compared to observations. However, when taking brightness temperature forecasts into consideration, the Thompson scheme displayed the best overall skill despite warmer cloud top brightness temperatures as compared to observations. Lastly, it was shown that all schemes underestimated midlevel clouds and overestimated clear sky conditions.

More closely related to the research presented herein, Jin et al. (2014) explored the effects of ice phase cloud microphysics on the prediction of TC environments using the Coupled Ocean-Atmosphere Mesoscale Prediction System-Tropical Cyclone (COAMPS-TC) model (Doyle et al. 2012). Output from simulations conducted using a single-moment (i.e., predicts only hydrometeor mass mixing ratios; Rutledge and Hobbs 1983) and hybrid double-moment (i.e., also predicts

total number concentration for selected variables; Thompson et al. 2008) were evaluated. This study used a multi-nested domain, with 45, 15, and 5-km horizontal grid spacing for the outer, intermediate, and inner domain respectively, and simulated fifteen Atlantic basin TCs of varying intensity from 2010 to 2011. Overall, the single-moment microphysical parameterization produced upper-level cloud ice up to two orders of magnitude greater than the hybrid double-moment parameterization. Additionally, longwave radiative heating at the base of the ice cloud layer in the single-moment-based simulations produced a 1-2°C warm bias compared to model-derived syntheses of observations. This bias was not found in the hybrid double-moment-based simulations. Furthermore, SSI brightness temperatures at 6.48 μm (water vapor channel) and 10.7 μm (longwave infrared channel) for Hurricane Igor (2010) were evaluated between the two microphysical schemes. The single-moment parameterization produced thick cloud ice over the domain that made the convective region associated with the hurricane indistinguishable. The hybrid double-moment parameterization clearly displayed Hurricane Igor, with the eyewall displaying brightness temperature values less than -60°C (213 K); however, unlike in observations, a uniform, tight eyewall was not produced.

d) Extratropical Transition

Extratropical transition, or ET, takes place when a TC moves into the midlatitudes and transforms into an extratropical cyclone, or one associated with frontal boundaries (Jones et al. 2003). Indications of ET can be seen via satellite when the symmetrical cloud distribution of a TC becomes increasingly asymmetric

(e.g., Figure 7). As the storm moves into higher latitudes, erosion of the eyewall can be seen as colder, drier air from higher latitudes wraps into the TC's left-rear quadrant. Concurrently, an extensive cirrus cloud shield, indicative of the TC's interaction with the upper tropospheric polar jet, and a delta-shaped region of convection associated with the isentropic ascent of warm, moist air above a region of lower to middle tropospheric frontogenesis form ahead of the transitioning cyclone (Figure 7b). ADT scene types often quickly go from the eye scene type, or a scene type with a moderate to high T#, to either curved band or shear scene types with low T#s during ET. This results in a rapid decrease in T# and, consequently, a rapid decrease in intensity estimates that is mitigated only partially by ADT (and DT) rules that constrain the rate at which intensity estimates are allowed to decay. As TCs approach the mid-latitudes, the maintenance of their intensity despite a rapid change from a symmetrical to asymmetric cloud structure is primarily driven by baroclinic energetics. As a result, the empirical relationships between cloud patterns and cyclone intensity underlying the DT and ADT no longer hold, resulting in the degradation of ADT-derived intensity estimates during ET (Olander and Velden 2007).

An attempt to obtain accurate intensity estimates of TCs during ET was made by Miller and Lander (1997), which utilizes the arc length of the primary outer cloud band not connected to the TC's center, the organization of the TC's low-level circulation, the existence of deep convection between the outer cloud band and the circulation center, and the translation speed of the storm to derive an "XT" number, which corresponds to an estimated wind speed value. A TC is deemed extratropical

when a loss of one-half or more of the central convection over the circulation center occurs as the storm maintains its forward motion or accelerates and/or the TC begins to move into a baroclinic zone and encounters strong vertical wind shear. After a storm is considered to be extratropical, the XT technique is performed, following the flowchart in Figure 8. This method, however, quickly failed to gain operational acceptance and the last known record of its operational use is in 1998 (Aldinger and Stapler 1998).

e) Extratropically Transitioning Storms Considered in this Work

i) Hurricane Edouard (1996)

Hurricane Edouard was the strongest tropical cyclone exhibited during the 1996 Atlantic season, maintaining a Category Three or greater intensity on the Saffir-Simpson Hurricane Wind Scale (Schott et al. 2012) for close to eight days (08/24 18Z – 09/01 06Z). The National Hurricane Center (NHC) best track (e.g., Jarvinen et al. 1984) for the times used in this study (08/30 18Z – 09/04 18Z) is shown in Figure 14a. NHC declared the storm extratropical on 09/03 06Z, where the storm exhibited a MSLP of 985 hPa and MSW of 55 kt (Pasch and Avila 1999).

ii) Hurricane Erin (2001)

Erin obtained hurricane status on September 8th 2001, where it quickly intensified from then, reaching a peak intensity of 105 kt the following day. Erin dabbled between a Category 2 to Category 3 hurricane (09/09 06Z – 09/10/18Z) as it maintained a relatively northward path just prior to the times of interest used in this report, with a sharp east-northeastward recurvature seen on September 11th (Figure 14b). An approaching strong upper-level trough caused Erin to accelerate

northeastward, where it eventually achieved ET status on 09/15 06Z, with a MSLP of 981 hPa and MSW of 60 kt (Beven et al. 2003).

iii) Hurricane Leslie (2012)

Leslie reached hurricane status on 09/05 06Z; however, the relatively slow forward motion of the storm resulted in significant upwelling of colder water underneath the storm that ultimately caused the storm to weaken back into a tropical storm on 09/07 12Z. As an emerging upper-level trough pushed off the east coast, Leslie was steered away from the cold, upwelled water, eventually reintensifying into a hurricane on September 10th 12Z before becoming extratropical on September 11th 9Z with a MSLP of 968 hPa and MSW of 65 kt (Stewart 2012).

iv) Hurricane Noel (2007)

Noel reached hurricane status and its peak intensity on 11/02 00Z. As it accelerated northeastward ahead of a mid-latitude trough, inner-core convection quickly weakened and the storm was deemed extratropical on 11/03 00Z. Noel exhibited a warm seclusion structure after ET, with minimum sea level pressure falling from 980 hPa on 11/03 00Z to 968 hPa on 11/05 12Z (Brennan et al. 2009).

v) Hurricane Ophelia (2011)

Ophelia became a hurricane around 09/29 18Z, reaching peak intensity of 120 kt close to 10/02 00Z, before strong south-westerly shear over cold water quickly acted to weaken the storm after achieving peak intensity (Avila and Stewart 2013). The storm was deemed extratropical on 10/03 10Z, at which time it

exhibited a 990 hPa minimum sea level pressure and 60 kt maximum sustained winds.

f) Cyclone Phase Space

A universal definition for ET does not exist within the meteorological community. Several methods exist by which the start and end of ET may be defined, including subjective assessment utilizing satellite imagery (e.g., Klein et al. 2000), potential vorticity metrics (e.g., Kofron et al. 2010), and an evaluation of cyclone asymmetry and thermal wind structure (e.g., Hart 2003). Herein, we describe the latter of these methods, the cyclone phase space of Hart (2003), which defines ET start and ET end based on three parameters: lower-tropospheric thermal asymmetry (B), lower-tropospheric thermal wind (cold versus warm core, ($-V^{L}_{T}$)), and upper-tropospheric thermal wind (cold versus warm core, ($-V^{U}_{T}$)).

The first parameter (B), uses the storm-motion-relative 900 – 600 hPa thickness asymmetry, centered on the storm track and calculated within a 500 km radius, to depict the magnitude of thermal structure asymmetry:

$$B = h(\overline{Z_{600hPa} - Z_{900hPa}}|_R - \overline{Z_{600\,hPa} - Z_{900\,hPa}}|_L) \quad (1)$$

Here, R denotes the hemisphere to the right of the current storm motion, L denotes the hemisphere to the left of the current storm motion, Z is isobaric height, and h is a placement value (+1 for Northern Hemisphere and -1 for Southern Hemisphere). Mature TCs will display a B value close to zero, indicating a thermally symmetric storm (Figure 9a). As a tropical cyclone approaches the mid-latitudes, colder air encroaches upon the cyclone poleward of the cyclone's track while warmer air becomes isolated equatorward of the cyclone's track. As a result, the 900 – 600 hPa

thickness continuously decreases poleward of the cyclone's track, resulting in increasing B values (Figure 9b). After examining 61 Atlantic TCs undergoing ET between 1979 and 1993 using 1.125° ECMWF reanalysis data, Evans and Hart (2003) subjectively determined B = 10 m to be the defining threshold between a tropical and transitioning or non-tropical cyclone, as no major hurricane with winds greater than 100 kt had a B value exceeding 10 m. Thus, a TC obtaining an asymmetry parameter B of greater than or equal to 10 m is said to mark the start of ET.

The remaining two parameters, $-V^{L}_{T}$ and $-V^{U}_{T}$, are both vertical derivatives of the maximum geopotential height gradient within 500 km of the cyclone center for the lower troposphere (900 hPa – 600 hPa) and upper troposphere (600 hPa – 300 hPa), respectively. Under the assumption of thermal wind balance, these parameters indicate whether a cyclone has a warm-core or a cold-core structure. In other words, if the magnitude of the isobaric height gradient above the cyclone increases with height, such that the cyclone's intensity increases with increasing height, the cyclone is defined as cold-core. If the isobaric height gradient decreases with height, such that the cyclone's intensity decreases with increasing height, the cyclone is defined as warm-core (Figure 10). Following Hart (2003), we define the cyclone height perturbation (ΔZ) evaluated within a 500km radius of storm center as

$$\Delta Z = Z_{max} - Z_{min}. \quad (2)$$

Further, ΔZ can be described as

$$\Delta Z = dg\left|\boldsymbol{V_g}\right|/f, \quad (3)$$

Here, d is the distance between the maximum and minimum geopotential height, *f* is the Coriolis parameter, g is the gravitational constant, and $|\mathbf{V}_g|$ is the magnitude of the geostrophic wind. Upon taking the vertical derivative of ΔZ with respect to the natural logarithm of pressure, bounded between the lower troposphere and upper troposphere, ΔZ becomes proportional to a scaled thermal wind, or

$$\left.\frac{\partial(\Delta Z)}{\partial \ln p}\right|_{900\ hPa}^{600\ hPa} = -|V_T^L| \quad (4)$$

and

$$\left.\frac{\partial(\Delta Z)}{\partial \ln p}\right|_{600\ hPa}^{300\ hPa} = -|V_T^U| \quad (5)$$

If the value of $-V_T$ is negative, where the magnitude of the cross-cyclone isobaric height gradient increases with height above the cyclone center, the TC is cold-core. Likewise, if $-V_T$ is positive, where the magnitude of the cross-cyclone isobaric height decreases with height, it is defined as warm-core (e.g., Figure 10). The end of ET is defined as the time at which the cyclone completes the transition from a warm-core to a cold-core structure within the lower troposphere (e.g., $-V_T^L < 0$). A classic example of an extratropical transitioning cyclone can be seen in Figure 11, displaying the cyclone phase space trajectory for North Atlantic Hurricane Floyd (1999).

III. Methodology

a) Model Configuration

Intensity time series (minimum sea level pressure and maximum sustained surface winds, in hPa and kt respectively) and SSI are obtained from numerical simulations of five observed ET events (Edouard (1996), Erin (2001), Noel (2007),

Ophelia (2011), and Leslie (2012), Figure 12,13) in the North Atlantic Ocean, with the storm tracks for each case displayed in Figure 14. Numerical simulations are conducted using version 3.4.1 of the Advanced Research version of the Weather Research and Forecasting (WRF-ARW; Skamarock et al. 2008) model. The TCs chosen both started and completed ET, as determined using the cyclone phase space of Hart (2003), and remained over water prior to completing ET. Initial and lateral boundary conditions for all numerical simulations are obtained using the European Centre for Medium-Range Weather Forecasts (ECMWF) Interim Reanalysis dataset with 0.7° latitude and longitude horizontal grid spacing (Dee et al. 2011). All simulations are of 120 h duration, ending approximately 24 h after the end of ET as determined from the National Hurricane Center "best track" historical record (Jarvinen et al. 1984), with hourly output. Within WRF-ARW, a horizontal grid spacing of 4 km was used with 30 vertical levels. All simulations used the Yonsei University (YSU) planetary boundary layer (PBL) parameterization, which parameterizes the sub-grid vertical transfer of mass, moisture, and energy between the surface and atmosphere (Hong et al. 2006). MM5 similarity (Section 2a of Jimenez et al. 2012), from which the model-derived maximum sustained surface wind is obtained, is used to parameterize surface-layer processes. The RRTMG scheme is used to parameterize longwave and shortwave radiation (Iacono et al. 2008). Deep, moist convection is treated explicitly within all simulations.

b) Microphysical Parameterization

Microphysical parameterizations numerically represent the microphysical processes that govern cloud particle formation, growth, and dissipation on very

small scales. Such processes include, but are not limited to, phase changes of water and interactions between cloud and precipitation particles of multiple forms (Stensrud 2007). The type of moment used (i.e., single-moment schemes that predict hydrometeor mass mixing ratios versus double-moment schemes which predict both the mass mixing ratios and total number concentration for each species) can have a significant effect on cloud development within a model, as demonstrated by the works of Jankov et al. (2011), Cintineo et al. (2014), and Jin et al. (2014). As a result, this research uses an ensemble of five microphysical parameterizations, including the WSM6, Thompson, Morrison, Milbrandt and Yau, and WDM6 schemes for each of the five TCs listed in Section 3a. Thus, a total of twenty-five simulations are conducted and evaluated.

The WSM6 parameterization is a single-moment scheme that predicts water vapor, cloud water, cloud ice, rain, snow, and graupel mass mixing ratios (Hong and Lim 2006). The Thompson parameterization is similar to the WSM6 scheme in that it is single-moment for water vapor, cloud water, snow, and graupel. In this parameterization, however, mixing ratios and number concentrations for both cloud ice and rain are predicted. This scheme was designed to improve forecasts of water phase particles at all altitudes and accumulated precipitation at the surface, incorporate recent microphysics observations from field projects, and to fulfill the requirements of real-time modeling needs in terms of computational efficiency (Thompson et al. 2008). The Morrison parameterization includes double-moment treatment of cloud droplets, cloud ice, snow, rain and graupel, and is single-moment for cloud water (Morrison et al. 2009). The Milbrandt and Yau, or simply Milbrandt,

parameterization is double-moment for all predictive variables (Milbrandt and Yau 2005). Lastly, the WDM6 parameterization (Lim and Hong 2010), which is based off the WSM6 microphysics scheme, is single-moment for ice, snow, and graupel, and double-moment for warm-rain processes (cloud water and rain). It also adds a prognostic variable of cloud condensation nuclei (CCN) number concentration. The prediction of number concentrations of clouds and rain in addition to the CCN distribution allows for flexibility in variable raindrop size distribution when forecasting thunderstorms in a computationally-efficient manner. The major difference between the WDM6 parameterization and other double-moment parameterizations (Thompson, Morrison, Milbrandt) is the addition of the prognostic equations for cloud water and CCN number concentrations. This allows for aerosols and their resulting effects on cloud properties and precipitation to be explicitly accounted for within a given numerical simulation. A succinct summary of the fundamental differences in how the WSM6, Thompson, and Morrison parameterizations are formulated is provided by van Weverberg et al. (2013).

c) Data Analysis

Model-derived intensity values and SSI derived from model output are obtained at every hour. SSI is derived utilizing a forward radiative transfer operator developed at the Cooperative Institute for Research in the Atmosphere (CIRA) at Colorado State University, following Grasso et al. (2014) and references therein. Hydrometeor particle sizes are computed utilizing assumptions inherent to each of the five microphysical parameterizations utilized in this study. We consider SSI obtained only for simulated GOES-12 channel 4, corresponding to the longwave

infrared window centered at 10.7 μm. ADT is employed on the SSI to obtain an ADT-estimated intensity at every hour. Using the time series of MSLP and MSW obtained at every hour from the numerical model as a proxy for "observed" intensity, and the hourly ADT intensity estimates, we perform an internally-consistent comparison between "observed" intensity values (or model "truth") and ADT-estimated intensity values, with an example of this provided in Figure 15. Furthermore, as the time duration between ET start and end can differ not only between individual ET events, but also for a given ET event simulated using different microphysical parameterizations, error statistics are computed using a normalized ET timeline, broken down into five distinct times: 24 hr prior to ET start (T_b – 24 h), 12 hr prior to ET start (T_b – 12 h), the start of ET (T_b), the mid-point of ET (T_{mid}), and the end of ET (T_e), each as determined using the cyclone phase space of Hart (2003). Figure 16 shows an example depicting ET start and end for the Leslie (2012) simulation conducted using the WSM6 microphysics scheme.

Lastly, we consider an alternative statistical approach to obtain storm intensity estimates using SSI. Here, the twenty-five cases, subdivided into five groups corresponding to their microphysical scheme, along with their respected model-derived ("truth") intensity values, are utilized. All SSI images are cropped within a 648 x 648 km square (with $\Delta x = \Delta y = 4$ km) centered on the model-derived storm center. Four out of five storms for each subgroup serve as training data and are appended to form an NxM matrix, with N equivalent to the total number of individual images sampled hourly and M equaling the total spatial points (161 x 161

= 25921). A composite-mean SSI image of the four storms is then created from the N images in the training data set.

The mean of the training dataset is then subtracted from each element of the training dataset, which is then subjected to an Emperical Orthogonal Function (EOF) analysis (e.g., Monahan et al. 2009) to identify spatial patterns that dominate variability in the TCs' simulated cloud structure. The overarching idea behind this methodology is that storm intensity is correlated to the instantaneous spatial cloud pattern of the storm. This is akin to both the DT and ADT except that it does not explicitly consider only purely tropical cloud pattern structures. The principle components (PCs) associated with the leading EOF modes, that both capture the majority of the storm's variance and are well-separated from the flat tail of the EOF spectrum, are used as predictors in the linear model for the model-derived ("truth") intensity I:

$$I = b_o + b_1 PC_1 + b_2 PC_2 + b_3 PC_3 + b_4 PC_4, \quad (6)$$

Here, $b_{\#}$ are the coefficients obtained via multiple linear regression by minimizing the root-mean-square distance between the right-hand side and left-hand side of (6) over all of N data points.

Finally, the storm structure anomalies of the single storm not used in the training dataset, with respect to the composite mean of the training set, are projected onto the leading four EOF patterns to derive magnitudes for the four leading PCs, with (6) thus providing an estimate of the storm's intensity at every hour. This process is repeated four times, once for each respective microphysics scheme, with each training dataset containing a new unique combination of four

TCs.

IV. Results

This section displays and analyzes model-derived minus ADT-estimated pressure and wind errors for each TC (as stratified by microphysical parameterization) and each microphysical parameterization (as stratified by TC). Synthetic satellite imagery, including its raw values and spatial organization, is analyzed to gain insight into the results. Finally, results obtained via the EOF method are shown and discussed.

a) Model-Derived ("Truth") minus ADT-Estimated Intensity Error Results

Sea level pressure (hPa) and wind (kt) differences for the same storm composed of different microphysical schemes for all times are shown are Figures 17 and 18, respectively. Model-derived minus ADT-estimated pressure (hPa) and wind (kt) for storms composed of the same microphysical scheme which are normalized to the ET timeline are displayed in Figures 19 and 20, with the same storm with differing microphysics schemes shown in Figures 21 and 22. Negative values on the pressure error graphs and positive values in the wind error graphs indicate ADT-estimated weak biases.

As 75% of DT-derived intensity estimates are within 12 kt of best track intensity (Brown and Franklin 2002), and given that ADT-derived intensity estimates are competitive with DT-derived intensity estimates (Olander and Velden 2007), similar results can reasonably be expected for the numerical simulations twenty-four hours prior to ET. The composite means for all storms within their respected microphysics scheme, except for the WSM6 and WDM6 cases, hold true to

this expectation, with nearly all estimates being weak-biased. Errors typically grow through time, including before and during ET, particularly for minimum sea level pressure. Several observations can be made from the graphs. First, Leslie displays the largest error differential between observed and estimated pressure and wind errors for nearly all times listed, indicative of a large weak bias for ADT estimates across all microphysical schemes (Figures 19, 20, 21c, 22c). Second, ADT estimates demonstrate a weak bias for all storms throughout all times using the WSM6 and WDM6 microphysics schemes (Figures 19a,b and 20a,b). The Thompson, Morrison, and Milbrandt cases contain several storms with a strong bias (ADT estimates stronger than model derived truth) twenty-four hours prior to ET start, most notably with Noel, which exhibits a 17.6, 21.6, and 20.5 hPa strong bias for the Thompson, Morrison, and Milbrandt cases respectively (Figure 19c,d,e and Figure 20c,d,e).

While the general weak bias that most cases display in the ADT-estimated intensity seen twenty-four hours prior to ET becomes larger during ET, the Ophelia Milbrandt-based simulation displays the opposite trend, exhibiting a strong bias twenty-four hours prior to ET that grows increasingly stronger as the storm approaches the end of ET (Figures 19e, 20e). Also worth noting is the Leslie Morrison-based simulation (Figures 19d, 20d), which displays the highest starting error out of all twenty-five storms, with the ADT-estimated minimum sea level pressure 57 hPa higher and ADT-estimated maximum sustained surface wind 71 kt lower than the model-derived estimates.

It should come as no surprise that a large discrepancy between model-

derived “truth” and ADT estimates for pressure values would be accompanied by large discrepancies between ADT-derived maximum sustained surface wind estimates and model-derived “truth.” However, unlike for minimum sea level pressure, which displays a gradual increase in error through time as displayed by the composite-mean in Figure 19, the composite mean for each microphysics scheme is increasingly weak-biased only until the start of ET (T_B) (Figure 20). A gradual decrease in the magnitude of this bias is noted at later times during ET. We hypothesize that this could reflect the evolving pressure-wind relationship for each transitioning TCs, where a given minimum sea level pressure corresponds to a weaker maximum sustained surface wind but larger expanse of gale-force winds during ET as compared to before ET (Evans and Hart 2008). Additionally, an initial strong bias can be found for several TCs simulated using the Thompson, Morrison, and Milbrandt schemes (Figure 20c,d,e). Lastly, much like what was found with the Ophelia Milbrandt-based simulation case for minimum sea-level pressure, wherein a strong bias was maintained through time, the wind error illustrates a similar trend (Figure 20e).

b) Model-Derived Tropical Storm Information

i) Edouard

Edouard (1996) achieves minimal hurricane intensity within the early stages of each simulation (Figure 13a). All microphysics schemes produce upper-level clouds over the TC throughout the majority of each simulation (Figure 23). The images depicted in Edouard and the following storms are meant to show the dominant spatial patterns of the storms leading up into ET start. This is important

as ADT must produce realistic intensity estimates leading up to ET start in order to ensure that ADT-estimated biases can reasonably be assessed during ET. The effects of moderate to strong vertical wind shear upon the cloud pattern organization of each simulated TC are apparent at this time, with cold brightness temperatures displaced to the north and east of the TC center and warm brightness temperatures organized in a circular fashion at the TC center. The start of ET on average takes place 67.6 hours post-simulation, with the shortest ET duration exhibited by the Morrison-based simulation at 22 hours and the longest by the Milbrandt-based simulation at 52 hours. The Morrison-based simulation is the weakest of the five, exhibiting a MSLP of 990 hPa at peak intensity (Figure 12a).

ii) Erin

Erin (2001) developed into a minimal hurricane within each simulation, with the highest recorded MSW values ranging between 79 to 82 kt approximately three days post-model start time or near the start of ET in each simulation (Figure 13b). Just prior to achieving the highest recorded MSW values, all five schemes exhibited a discernable (if partially open) eye in SSI, as illustrated in Figure 24, with an eye lasting up until around ET start. Mean ET duration between the five storms lasted on average of 28.2 hrs.

iii) Leslie

Leslie (2012), the strongest of the five storms in both reality and model simulations, has MSW values peaking between 97 – 108 kt across the five schemes near the start of ET (Figure 13c), which takes place on average 88.6 hours after simulation start. A large eye is seen leading up to ET start in all simulations (Figure

25), with an eye forming as early as 26 hours post simulation start for the WSM6-based simulation and as late as 58 hours post simulation start in the Thompson-based simulation. The large eye structure dissipated in each case towards the end of ET. The ET process was quick for all simulations, only lasting 15 hours on average from start to finish, presumably due in large part to the synoptic-scale environment supporting ET (Hart et al. 2006), e.g., the meridional advection of Hurricane Leslie relative to the more zonally advected storms (Figure 13c).

iv) Noel

Noel (2007) briefly developed into a Saffir-Simpson Hurricane Wind Scale (Schott et al. 2012) Category 2 hurricane within the WSM6 microphysics-based simulation, exhibiting 90 kt winds approximately three days post model start time. The simulated Noel (2007) was slightly weaker at its peak intensity within the remaining four simulations of this case (Figure 13d). Unlike Erin and Leslie, Noel does not develop a discernable eye within any of the five simulations, as seen in Figure 26, which displays the SSI for Noel on 11/02 00Z, or 48 hours after the simulation start time. The extent of spatial cloud coverage plays an important role in ADT-estimates seen in this report, as discussed in section 5. The WSM6- and WDM6-based simulations produce a feature similar to that of a CDO or irregular CDO ADT scene (Figure 26,a,b), with extensive middle- to upper-level clouds seen north and northeast of the storm. The Thompson-based simulation is similar, with a larger aerial extent of cloud cover seen over storm center (Figure 26c). Lastly, more extensive upper-level cloud cover (associated with colder brightness temperatures) can be seen for Noel in the Morrison- and Milbrandt-based simulations (Figures

26d,e). ET begins 61 – 66 hours post model start time, with an average ET duration of 38.8 hours (vertical dashed lines in Figures 12e and 13e).

v) Ophelia

The Ophelia (2011) Thompson- and Morrison-based simulations do not produce an intense storm. We hypothesize this to be in part due to strong environmental vertical wind shear (e.g., 15-20 m s^{-1} in the 850-300 hPa layer at 0000 UTC 2 October 2011, near the time of the observed TC's peak intensity, as diagnosed from the ERA-Interim reanalysis; not shown) and its influences on parameterized microphysical processes. The result is higher pressure and weaker wind speeds in both cases (Figures 12e and 13e). The simulated Ophelia in the remaining three cases (WSM6, Milbrandt, and WDM6) are more intense but differ in how each TC's structure evolves through time (Figure 27). The WSM6-based simulation is the strongest of the three Ophelia schemes, reaching major hurricane intensity with 105 kt winds, 62 hours into the simulation, or 14 hours post ET-start (Figure 13e). Additionally, it is the only storm of the three to produce a discernable eye (Figure 27a). The WSM6-based simulation also exhibits the longest duration of ET out of the three storms, lasting 42 hours. The Milbrandt-based simulation exhibits an intense and large CDO region, with cold cloud top temperatures (approximately -78° C or 195° K) throughout most of the model's lifecycle (Figure 27c), before exhibiting classic extratropical cloud features towards the end of ET (not pictured). This simulated storm develops into a minimal hurricane and exhibits its strongest winds (78 knots) three days into the simulation (Figure 13e), with ET lasting 23 hours. The WDM6-based simulation primarily exhibits CDO and irregular

CDO-like cloud organization for most of the storm's lifecycle (Figure 27b); however, brief bouts of an eye can be seen for a few hours approximately two days and again four days into the simulation (not pictured). While the areal extent of cold cloud top temperatures is not as extensive as in the Milbrandt-based simulation, the simulated cyclone nevertheless achieves a similar peak intensity (Figure 13e) and ET duration (23 hours).

c) Synthetic Satellite Imagery Brightness Temperatures

i) WSM6 & WDM6

The WSM6 and WDM6 schemes display the warmest cloud top temperatures on average between the five microphysical schemes used in this report, as seen from the collection of Hovmöller-style histograms in Figures 28a,b-32a,b. Differences in brightness temperatures can be see between the WSM6 and WDM6 scheme; however, these differences are subtle compared to those between WSM6/WDM6 and the remaining three microphysical schemes. After the first twelve hours of each model simulation (e.g., the model "spin up" period), brightness temperatures are most commonly between 190 K (Noel – Figures 31a,b) and 230 K (Ophelia – Figures 32a,b). However, it should be noted that cloud top brightness temperatures were not consistently contained within this range, as the histogram indicates instances of cloud top brightness temperatures >220 K for multiple TCs, as noted by the wide swatch of dark blue within the first two to three days of each simulation (Figures 28a,b-32a,b). We hypothesize this to be reflective of less expansive cold cloud top brightness temperatures within 200 km of the center of each TC, as can be inferred from Figures 23a,b-27a,b, and, in selected cases, the presence of an eye. Though not

unique to the WSM6- and WDM6-based simulations, ET is well-defined within each case's histogram by the rapid loss of cold brightness temperatures and concordant rapid increase in warm brightness temperatures within one to two days of the end of each simulation (Figures 28 – 32).

Van Weverberg et al. (2013) and Grasso et al. (2014) pose hypotheses as to why the areal extent of cold cloud top brightness temperatures is reduced in WSM6-based numerical simulations of continental and tropical mesoscale convective systems, respectively, as compared to simulations conducted using other microphysical parameterizations. Van Weverberg et al. (2013) hypothesize that the WSM6 parameterization produces too much ice with large diameters that falls out quickly. As cloud ice has been shown to be the predominant contributor to the coldest brightness temperatures obtained from SSI (e.g., Grasso and Greenwald 2004), the concordant reduction of cloud ice aloft results in warmer cloud top brightness temperatures. Conversely, Grasso et al. (2014) suggest that there is too much accretion of ice by snow within the WSM6 parameterization, with the snow then falling out at a relatively fast fall velocity, thus resulting in reduced ice and warmer cloud top brightness temperatures. Further investigation is necessary, however, to deduce which – if either – of these two hypotheses holds for the transitioning TC cases examined herein. Lastly, WDM6 handles ice identically to the WSM6 scheme, which we hypothesize is likely responsible for the similar brightness characteristics between the two (Van Weverberg et al. 2013).

ii) Thompson

The Thompson scheme consistently produces a wide areal extent of cold

cloud top brightness temperatures, as illustrated by the green, yellow, and red in the histograms (Figures 28c-32c), with most common brightness temperatures again between 190 K (Noel – Figure 31c) and 230 K (Erin – Figure 29c). The histograms help illustrate differences in simulated storm structure between each of the cases considered; simulated TCs with an expansive CDO have a greater concentration of cold brightness temperatures (and few warmer brightness temperatures) within 200 km whereas simulated TCs with eyes have a broader range of brightness temperatures, both cold (deep, moist convection) and warm (inside the eye), within 200 km. For instance, the Thompson-based Leslie simulation starts off with a CDO scene type, producing over 1000 pixels with cloud top temperatures < 200 K, but as the eye develops we start to see a decrease in pixels with cold cloud top brightness temperatures. Concurrently, and consequently, we see brightness temperatures greater than 280 K appear on the histogram, indicative of the sea surface temperatures within the cloud-free (or nearly so) eye.

Unlike the WSM6 and WDM6 scheme, the Thompson scheme includes a size threshold (200 microns) for cloud ice, with excess ice converted to snow. As a result, the Thompson scheme normally produces more snow in the upper troposphere with a large number concentration and smaller falling velocity (Van Weverberg et al, 2013). In van Weverberg et al. (2013), it was found that both snow and cloud ice fell slower relative to the WSM6 and Morrison schemes, and as a result there was much more ice and snow buildup aloft. We hypothesize that this is what occurs within our simulations, resulting in plentiful cold cloud top temperatures. We note that brightness temperature differences between the Thompson and WSM6/WDM6

schemes, in addition to the Morrison and Milbrandt schemes, are likely also a function of how each scheme parameterizes ice nucleation, such as was illustrated by Jin et al. (2014).

iii) Morrison

The Morrison scheme produces cloud top temperatures values comparable to the Thompson scheme for each TC (Figures 28d-32d), albeit generally with a slightly larger range of brightness temperatures over which the coldest brightness temperatures are found. Like the Thompson scheme, the Morrison scheme includes a size threshold for cloud ice, with the portion of cloud ice larger than the threshold automatically transferred into snow. It should be noted that the maximum ice number concentration allowed in the Morrison scheme is 10 cm^{-3}, a much larger threshold compared to the 0.25 cm^{-3} allowed by the Thompson scheme (Cintineo et al. 2014), which is thought to result in a wider areal extent of upper-level clouds prior to ET (e.g., Figures 23d-26d). Furthermore, unlike the WSM6, WDM6, and Thompson schemes, the Morrison scheme explicitly predicts the number concentration for snow. Van Weverberg et al. (2013) noted that explicitly solving for the number concentration for snow in MCSs led to snow with large diameters and faster fall velocities – and, consequently, fewer snowflakes – in the middle troposphere. It should be noted, however, that van Weverberg et al. (2013) studied tropical MCSs whereas transitioning TCs are the focus of this work. As a result, further investigation is needed to confirm whether the same processes seen in the van Weverberg et al. (2013) study are at play within the cases considered herein.

iv) Milbrandt

The Milbrandt scheme produces the coldest cloud top brightness temperatures, with most common cloud top brightness temperatures between 185 – 210 K (Figures 28e-32e). Much like the Morrison scheme, the Milbrandt scheme simulates extensive areas of upper-level clouds relative to the WSM6/WDM6 and Thompson cases (Figures –23e-26e, 27c), which is not surprising as the Milbrandt scheme uses the same maximum ice number concentration (10 cm^{-3}) as the Morrison scheme. Ice nucleation is formulated using the empirical formula of Meyers et al. (1992). Cintineo et al. (2014), in their study of continental severe thunderstorm events, found that the Milbrandt scheme (and, to a lesser extent, Morrison scheme) overpredict high cloud cover (and thus cold brightness temperature) coverage. They hypothesize that relatively vigorous vertical transport of cloud condensate, relatively slow fall velocities, and relatively small particle diameters within their Milbrandt-based simulations (as compared to their WDM6-based simulations in particular) may be the result of this overprediction. Though further investigation is warranted, this is a plausible explanation for the differences seen herein.

d) Empirical Orthogonal Function Analysis

A varying amount of skill can be seen in the final results for the EOF analysis when used to predict tropical storm estimates, both pre, during, and post-ET (Figure 33). Visually, the Ophelia Milbrandt-based application shows the most skill throughout all times, capturing the increasing intensity trend pre-ET start and the decreasing trend post-ET start (Figure 33e). The Edouard Morrison-based application has the hardest time capturing the intensity for most time-steps (Figure

33a). This is most likely due to the Edouard Morrison-based simulation exhibiting shearing and thus displaced cloud tops throughout the middle of the simulation, in contrast to the spatial patterns that dominate variability in the training dataset's simulated cloud structures. The opposite can likely be said for Ophelia Milbrandt. The remaining storms, Erin (Thompson), Noel (WDM6), and Leslie (WSM6) capture the general increasing and decreasing intensity trend observed; however, clear discrepancies between model-derived truth and estimated intensity can be seen (Figure 33b,c,d). An example of a composite mean for the training dataset (which is used to derived storm structure anomalies of the single storm not used in the training dataset, or in this particular case, Ophelia Milbrandt, that is then projected onto the leading four EOF patterns) is shown in Figure 34, with the variance associated with each mode of EOF for the training dataset shown in Figure 35. The first four EOF modes were used in every case as they accounted for the most variability within each dataset, capturing anywhere between 62% to 78% of the total variance. The predictors used to determine the b coefficients found using multiple linear regression are pictured in Figure 36. Lastly, the spatial patterns of the first four EOFs used in predicting the intensity of Ophelia Milbrandt are shown in Figure 37.

V) Discussion

At first glance, the composite mean throughout time normalized to the ET timeline seem to give relatively reasonable error values given that the very small amount of actual cases of ADT-derived intensity estimates that we do have (Section 1) are 8.47 hPa and 13.12 kt too weak for minimum sea level pressure and

maximum 10-m wind speed, respectively, compared to real-life observations. However, given the large standard deviation from the mean between different storms with like-microphysical schemes (Figure 19,20) and to a lesser extent between similar storms with differing microphysical schemes (Figure 21,22) alike, along with the specific model-derived ("truth") minus ADT-estimated intensity error trends noted in section 4a, further investigation was warranted.

Three main components are thought to have the largest effect on the scene type and corresponding intensity values issued by ADT in this report: model-derived storm center, ADT-automated derived storm center, and cloud coverage and brightness temperatures.

Model-derived storm center was defined using the lowest recorded MSLP at every time-step. However, a limitation to this method came with the high resolution grid spacing used in this report, which resolved localized areas of MSLP minima within the eye of each hurricane that did not necessarily correspond precisely to the center of the simulated eye for those cases in which an eye was simulated. This is problematic for storms that did not produce a T# above 3.5, which fails to trigger the ADT auto-centering technique.

An ADT-derived storm center was often not triggered for storms that did display a final T# above 3.5-4.5, thus relying on the model-derived storm center, which is used by ADT as the final storm center if the an ADT-derived storm center cannot be used. It is believe that either a lack in spiraling signature in the SSI or the initial first guess (model-derived storm center) bring too far separated from the ADT-derived storm centering method are responsible in the ADT-centering method

not being used for final T#'s above 4.5.

Lastly, and thought to be the most important element, are cloud brightness temperatures and the extent of the spatial structure for CDO scene types, which play a major role in determining both scene type and intensity values.

a) WSM6/WDM6 weak bias

An ADT-estimated weak bias is shown for every storm using the WSM6/WDM6 microphysics schemes throughout all times, both prior and post ET (Figure 17, 18). It is vital to capture realistic scene types and ADT estimates prior to ET in order to capture realistic error intensities post-ET, however, this does not happen for WSM6 or WDM6, in any scenario. Throughout most times, the curved band and shear scene types, two of the weakest scheme types utilized by ADT, are dominant throughout all simulation, despite a clearly visible eye displayed in the SSI for Erin, Ophelia, and Leslie (WSM6, Figures 24a,25a,27a) and Erin and Leslie (WDM6, Figures 24b,25b) Additionally, the Noel and Edouard WSM6- and WDM6-based simulations (Figures 23a,26a and 23b ,26b), and Ophelia WDM6 (Figure 27b) display what seems to be representative of either a CDO/irregular CDO scheme type. Regardless, the weaker curved band/shear scene types are issued by ADT during these times. It is believed that warm cloud top temperatures relative to the Thompson, Morrison, and Milbrandt cases, along with non-uniform cloud top temperatures surrounding the storm center, are the main causes for triggering the weaker scene types, despite what is subjectively evident in SSI.

A good example can be seen in the Ophelia WSM6-based simulation, a case that correctly identifies the storm center at all time steps using the model-derived

storm center. It is believed that the lack of cold, uniform eyewall cloud top temperatures are playing a major role in the scene type. The lack of a symmetric, cold annulus region surrounding the eye produces a lower average cloud top temperature bounded within the 80 km-wide annulus centered region from storm center, which consequently produces a warm ΔT value. Additionally, the storm is likely deemed as "non-symmetrical", following the procedures in determining sym_{cloud}, described in section 2b and Figure 6b, also caused by variable cloud top temperatures surrounding the eye. These two parameter checks essentially lower the T# to the point where it "tricks" ADT into thinking it is looking at a developing or weakly sheared storm, causing an eye scene type (if issued during the first steps of the scene score process) to be disregarded, with curved band or shear scene types used in its place. An example of an image that was issued a curved band scene type despite an eye notably visible in SSI can be seen in Figure 38.

It is interesting to note the drastic reduction in error observed in the Ophelia WSM6 case that took place from ET mid to ET end. This is one of the only instances where an eye scene type was captured by ADT within the WSM6/WDM6 scheme (Leslie WSM6 briefly saw a few hours of an eye scene type), most likely due to a more consistent gradient of cloud top temperatures captured within the annulus region (Figure 39) relative to the previous hourly images. The eye scene is captured for a total of nine hours, which quickly brought ADT estimates from 996.1 hPa to 976 mb, allowing ADT estimates to draw closer to model-derived estimates (which were at 951 and 952 hPa respectively). This is also the only instance within the WSM6- and WDM6-based simulations that triggered the ADT-automated centering

mechanism, although no major changes to the CI# or ADT-estimated intensities were found when comparing it to the same case with only model-derived storm centers being used.

Last, the Ophelia WSM6-based simulation is also a decent example to why ADT-estimates often show a weak bias during ET in real life. The shift from a symmetrical storm with an eye to a non-symmetrical storm with a large expansion of clouds northward from storm center, and a lack of clouds west and south from storm center due to cold, descending air, can quickly cause eye scene types to shift straight into curved band/shear scene types, causing a rapid decrease in estimated storm intensity. This is easily seen when viewing the 136 km radius centered on storm center that ADT uses to determine the initial scene score. Notice the eye and surrounding eyewall is captured within the 136km window within ADT, with a rapid degeneration of the eye and outward displacement of remaining deep, moist convection during ET causing the shear scene type to quickly take the place of an eye scene type (Figures 40,41).

Storms that do not form a visible eye (Noel and Edouard for WSM6, Noel, Ophelia, and Edouard for WDM6) are also inferred to be primarily curved band and/or shear scene types by ADT. The Noel and Edouard WSM6- and WDM6-based simulations display most of the spatial extent of their clouds to the north and east of storm center (not pictured), either due to upper-level wind shear or a misplaced storm center, resulting in the producing of mainly curved band and shear scene types. The Ophelia WDM6-based simulation does produce clouds directly over the storm center, sparking some irregular CDO scene types; however, the curved band

and shear scene type continued to be the most dominant within this case despite the 136 km ADT search radius capturing the extent of the clouds. This most likely stems from the sym_{cloud} parameter deeming the TC to be highly non-symmetrical due to the lack of uniform cloud top temperatures, thus triggering the curved band and/or shear scene types.

The warmer temperatures seen in the SSI, relative to the other three microphysical schemes, produced final T#s below 3.5 for all cases except the Ophelia WSM6 (as discussed above), and in turn failed to trigger the ADT automated centering schemes. As a result, model-derived storm centers were used for ADT, and as mentioned previous, not all model-derived storm centers corresponded exactly with actual storm centers.

An example can be seen in the Erin WSM6-based simulation, with the sea level pressure minimum located slightly northwest relative to the center of the observed eye (as highlighted by Figure 42, which places a 136 km circle employed by ADT to derive scene scores, centered over the model-derived storm center). The displacement from actual storm center limits what the ADT is looking at during each time. For example, in Figure 42 (left), with a correct storm center, ADT potentially could have correctly distinguished this as an eye scene type, however, due to essentially only part of the picture being seen, an irregular CDO, curved band, or shear scene type are in the range of possibilities. In this instance, curved band was assigned to the storm at that hour. This displacement highlights the potential sensitivities observed when storm center is not correctly identified or is not collocated with the center of the cloud-free region associated with the eye. However,

it is thought that cloud top temperatures play the biggest role with the weak-bias observed for all cases simulated using the WSM6 and WDM6 parameterizations, as cases that were correctly centered (e.g. Ophelia WSM6, Ophelia WDM6) still managed to produce curved band/shear scene types for most times. However, erroneous storm centers are not to be ignored as they play a larger role in incorrectly determining scene type for cases such as Leslie.

b) Leslie weak-bias

The extreme weak-biases seen for Leslie across all microphysical scheme is due to an incorrect storm center location in conjunction with the fact that it was the strongest of the five storms, leading to large discrepancies between model-derived truth and ADT-estimated values. The Leslie Thompson-, Morrison-, Milbrandt-, and WDM6-based simulations exhibit a storm center displaced to the northwest of the eye (Figures 43a,b,c,d), in turn producing mainly CDO, irregular CDO, curved band and shear scene types leading up to ET start and primarily curved band and shear scene types at later times. The colder cloud top temperatures did produce final T#'s above 3.5 in both the Thompson- and Morrison-based simulations; however, the ADT autocentering technique did not prompt in these cases. The Milbrandt-based simulation does produce final T#'s above 4.5, in which the autocentering technique was successfully employed for several times pre-ET; however, even with the ADT-technique, the eye is still unsuccessfully captured for all but a few hours, resulting in mainly CDO and curved band scene types being employed. This does prompt the possibility that the eye is perhaps too large for ADT to successfully issue an eye scene type. Within the 136 km search window and an 80 km annulus fit to the TC

center region, assuming a correctly centered storm position, ADT will see mainly warm temperatures (e.g., sea surface temperatures), due to a lack of clouds within the eye. This in turn may issue a curved band scene type. Although this was not explicitly seen in this study, it is not outside the realm of possibilities.

c) Strong biases in Thompson, Morrison & Milbrandt schemes

The strong biases seen for the Thompson-, Morrison-, and Milbrandt-based simulations, especially twenty-four hours prior to ET, are caused by the storms that displayed a cold, expansive area of cloud top temperatures, as discussed in section 4c. This strong bias can be seen prior to T_B-24, as seen in Figure 19d,e and Figure 20d,e). Using Noel as an example, ADT displays mainly uniform and embedded center scene types prior to ET start. The cold, uniform temperatures seen by ADT bolsters high cold T_{cloud} values, low sym_{cloud} values, and depending on the extent of spatial coverage of the CDO scene types, large R_{cdo} values, all of which increase intensity estimates. This is certainly the case for the Noel Thompson-, Morrison-, and Milbrandt-based simulations. As ET takes place and clouds start to take a more asymmetric shape, the CDO and embedded center shear scene types quickly convert to curved band and shear (for similar reasons as discussed with the Ophelia WSM6-based simulation, Figures 40 and 41), responsible for the decreasing warm bias seen with Noel and the other schemes that display a warm bias.

The exception to this is the Ophelia Milbrandt-based simulation, the only case of the twenty-five that starts off with a strong bias twenty-four hours prior to ET and displays an increasingly strong bias post-ET (Figure 19e, 20e). This case exhibits very cold cloud top temperatures (~180 K) along with an expanding spatial

extent of clouds, causing both a cold T_{cloud} and large R_{cdo} to produce every increasing ADT-estimates as the storm approaches the middle of ET. The storm retains a fairly robust amount of cold cloud tops through ET, resulting in the continuous strong bias, unlike a case like the Noel Milbrandt-based simulation, which also displayed an anomalous amount of cold cloud top temperatures (Figure 26e), but quickly starts to display classic ET cloud features towards the start of ET, results in a diminishing strong bias at this time.

d) EOF analysis results

The EOF analysis does a surprisingly good job capturing estimated intensity values, in particular in capturing the increasing and decreasing intensity trends displayed by the observed intensity. Visually, the Ophelia Milbrandt-based application (Figure 33e) displays the most skill through time while the Edouard Morrison-based application (Figure 33a) displays little skill. Taking a look at the composite mean for the Leslie case (Figure 34), colder cloud top temperatures are seen north of the storm center, becoming progressively warmer towards the south. This should not come as much of a surprise as cold cloud top temperatures were seen north and east of the storm as it transitioned from a TC into an extratropical cyclone (Figures 23-26e, 27c). The composite mean was relatively similar between other cases (not pictured). The spatial patterns for the training dataset used to help derive Ophelia-Milbrandt estimates show a hurricane-like spatial pattern (EOF-1, which accounts for 45.3% of the variability), an extratropical pattern (EOF-2, which accounts for over 21.3% of the variability), a transitioning phase between and tropical and extratropical phases (EOF-3, 7.5% variability), and an eye pattern

(EOF-4, 3.9% variability). The spatial patterns are depicted in Figure 37, with the spatial patterns for the four other cases (not pictured) showing fairly similar patterns between the four modes. The one exception is with the training dataset used to predict Leslie (WSM6), which displays the extratropical pattern for mode-1 and the hurricane pattern for mode-2. The mean of Ophelia (not pictured) is fairly similar to the composite mean of the training dataset, and thus the EOFs used to derive storm estimated intensities are most likely well-correlated with the patterns seen in the Ophelia Milbrandt-based application through time, resulting in highly accurate intensity estimates.

The Edouard Morrison-based application (Figure 33a) likely fails to capture accurate storm intensities through time as it displayed some shearing mid-simulation, resulting in spatial patterns that are not well-correlated with the EOF modes derived in the training dataset. The remaining three schemes (Figure 33b,c,d) do fairly well at capturing the general increasing and decreasing intensity trends, with a strong estimated bias seen early in the simulation (a likely effect of model spin-up), and a weak bias seen mid-simulation (with the exception of the Thompson-based application which demonstrates a strong bias through most of the simulation). While the EOF method to derive storm intensities shows promise, it is not without its limitations. First, the training dataset for each case is relatively small, which greatly influences the estimated intensities being derived. For example, if the training dataset is mainly composed of storms that displayed an eye throughout most of the storms' lifecycle and is being used to estimate intensity for an independent case that predominantly exhibits a layer of clouds covering the eye,

results may be skewed due to the leading EOF modes projected on storm anomalies not correctly capturing the structural variation associated with each storm. Additionally, the Thompson- and Morrison-based applications both used storms in the training dataset that exhibited moderate to considerable shearing throughout the storms lifecycle, which influenced the composite mean and possibly the EOF spatial patterns used to derive storm intensities, although these cases still do a decent job capturing the up and down trends of the observed intensity.

One of the advantages the EOF method has on the ADT method is it is not so reliant on storm-center location, as it captures spatial variability over a large grid (648 by 648 km), whereas the ADT method mainly derives its scene type and thus intensity values within a 136 km search radius from model or ADT derived storm center, as was discussed previous.

VI. Conclusion

Herein, two methods of obtaining TC intensity estimates during ET using synthetic satellite imagery have been evaluated. In so doing, a few fundamental issues were observed that resulted in ET intensity estimation errors that are not thought to physically realistic. The WSM6 and WDM6 microphysics schemes failed to produce cloud tops that were cold enough to trigger the appropriate scene type prior to the start of ET. The lack of a tight, symmetrical eyewall containing like-temperatures for cases such as Erin and Leslie also proved problematic for triggering appropriate scene types (mainly the eye scene type) prior to ET. The strong biases seen in many of the Thompson, Morrison, and Milbrandt microphysics schemes are an artifact of the overproduction of ice-containing clouds in the upper

troposphere and, accordingly, cold cloud top temperatures (< 210 K), that also led to discrepancies between the model-derived "truth" and ADT-on-SSI-estimated intensities prior to ET. Additionally, several instances of incorrect storm centers can lead to large error discrepancies, as was seen for several of the Leslie storms. That said, it must be kept in mind that methods such as the DT and ADT are imperfect, with 50% of DT-derived TC intensity estimates differing from *in situ* observations by greater than 5 kt (Brown and Franklin 2002) and both ADT and DT-derived intensity estimates becoming less reliable during ET (Velden et al. 2006).

The estimated intensity values derived from the EOF analysis captured the general increasing and decreasing intensity derived from the model, especially in predicting Ophelia,. However, a lack of sample size in the training dataset is thought to be one of the possible reasons behind discrepancies between EOF-model-predicted and WRF-predicted intensities seen in the graphs and necessitates further study with larger datasets before the applicability of this method to observed storms can be evaluated. Storms that displayed cloud patterns indicative of upper-level shearing that were included in the training dataset also is a possible cause in the discrepancies seen in the final result, although estimated intensities still captured the increasing and decreasing trends of the model-derived ("truth") intensities.

Despite the issues noted in deriving errors and biases normalized to the ET timeline, insight on using SSI in replicating the spatial structure and cloud top temperatures during the transition of a tropical cyclone to an extratropical storm was gained. In general, SSI is promising in a qualitative sense as it seems to depict

the general cloud structures of each cyclone, more so for the WSM6, WDM6, and Thompson cases. In a quantitative sense, however, it is possible that these schemes do not sufficiently replicate the storm structure to a point where ADT can be used successfully leading up to the start of ET. While an extensive, in-depth analysis was not performed in this study, the results seen in this report closely follow the results seen in Cintineo et al. (2014), van Weverberg et al. (2013), and Grasso et al. (2014). In particular, the WSM6 and WDM6 produce warmer cloud top temperatures, hypothesized to be caused by the large buildup of ice that rapidly falls out of the storm. The Milbrandt and Morrison cases also exhibit properties observed in Cintineo et al. (2014) and Van Weverberg et al. (2013), in particular noting the colder cloud top temperatures and expansive spatial extent of cloud cover.

The overarching goal of this work and future work is to derive errors and biases seen during ET, and to use those values as the basis to create a relationship between cloud patterns and extratropical cyclone intensity, whether that be from deriving a new scene type, employing a new constraint or modified decay factor ,or perhaps by exploring and creating alternative methods not employed within ADT.

FIGURES

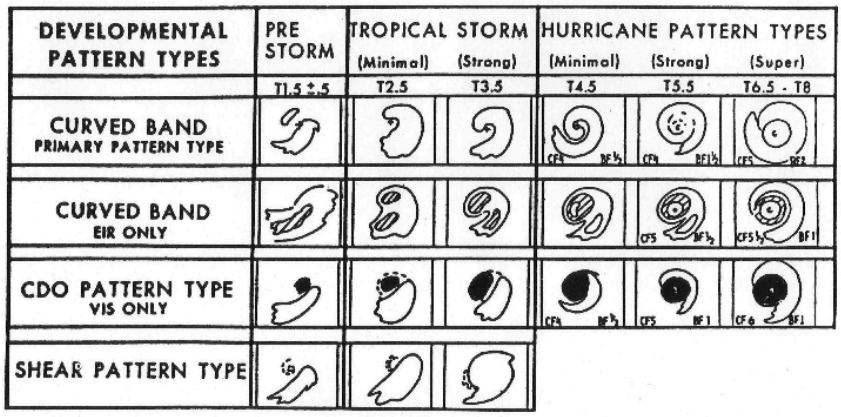

Figure 1: Developmental cloud pattern types used in intensity analysis. Pattern changes from left to right, corresponding to 1 "T" number per column, are typical twenty-four-hourly changes. Figure reproduced from Dvorak (1984), their Figure 5.

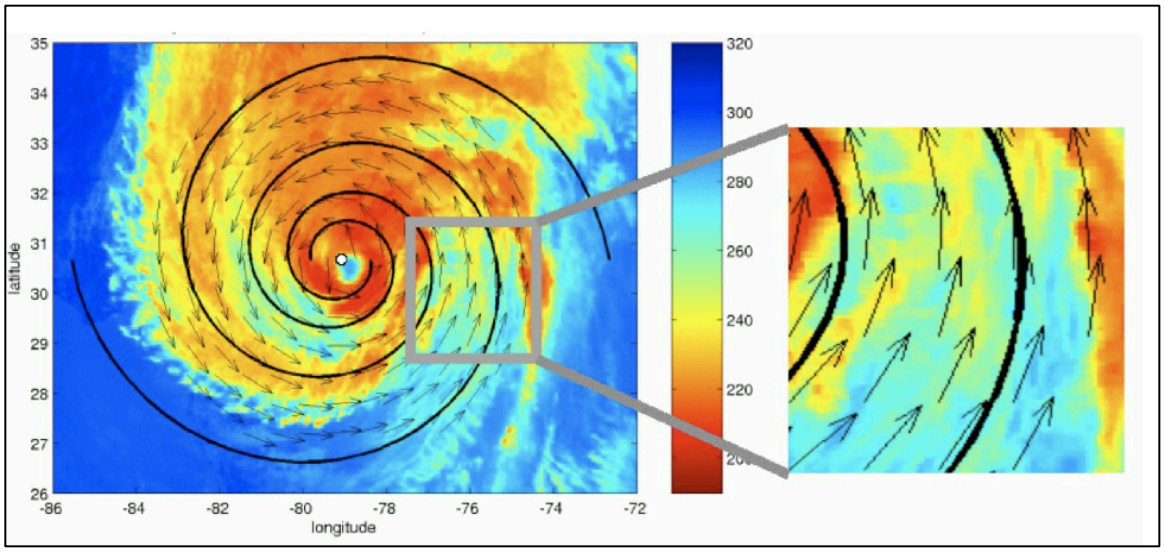

Figure 2: Example of a 5 –degree log spiral field vector field, used in the SC method, with the black lines originated from a test center point (white dot). Reproduced from the ADT Users' Guide Version 8.1.4, their Figure 7.

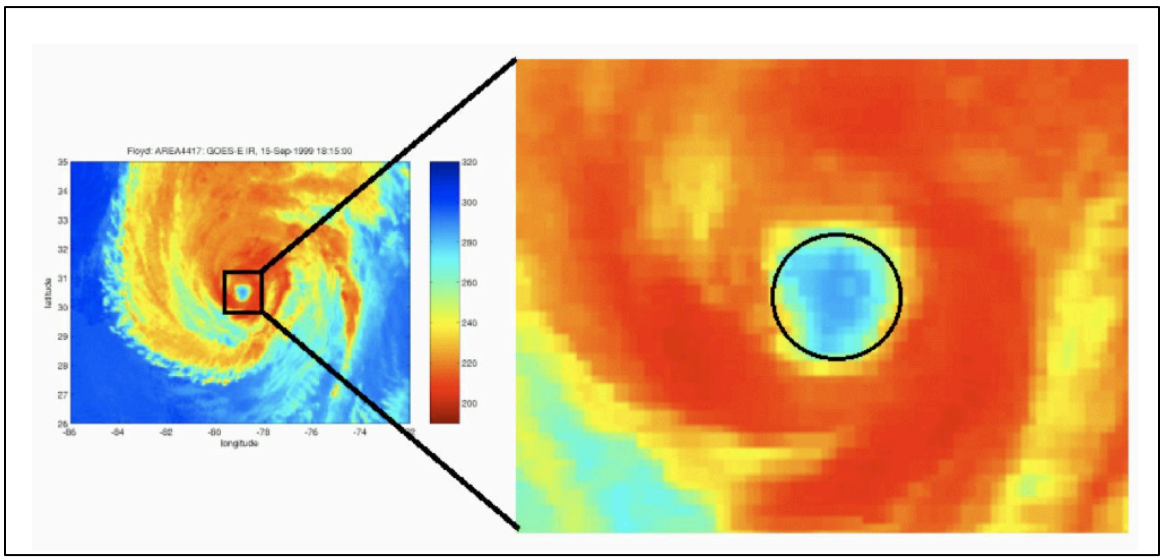

Figure 3: Example of the eye ring analysis used in the RF method, which best matches the temperature gradient of the eyewall. Reproduced from the ADT Users' Guide Version 8.1.4, their Figure 8.

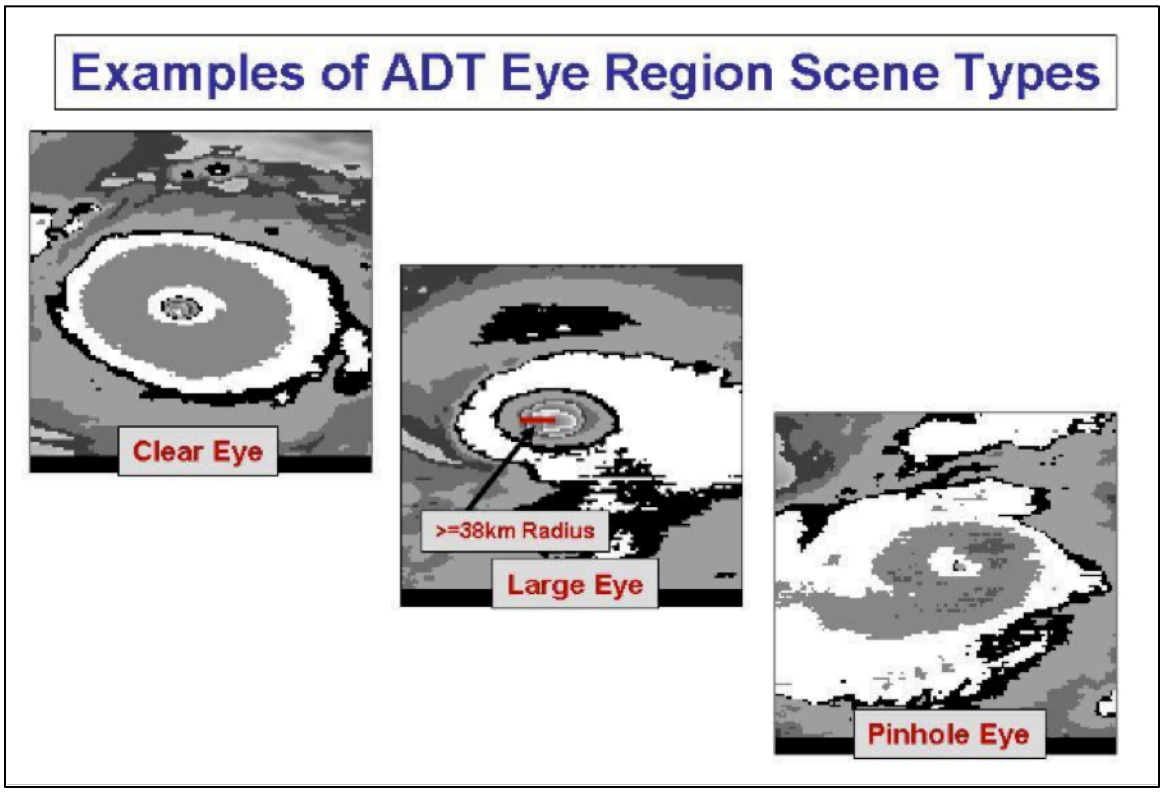

Figure 4: Examples of three ADT eye region scene types, corresponding to a clear eye (left), large eye (radius ≥ 38 km; center), and pinhole eye (right). Reproduced from Olander and Velden (2013), their Figure 3.

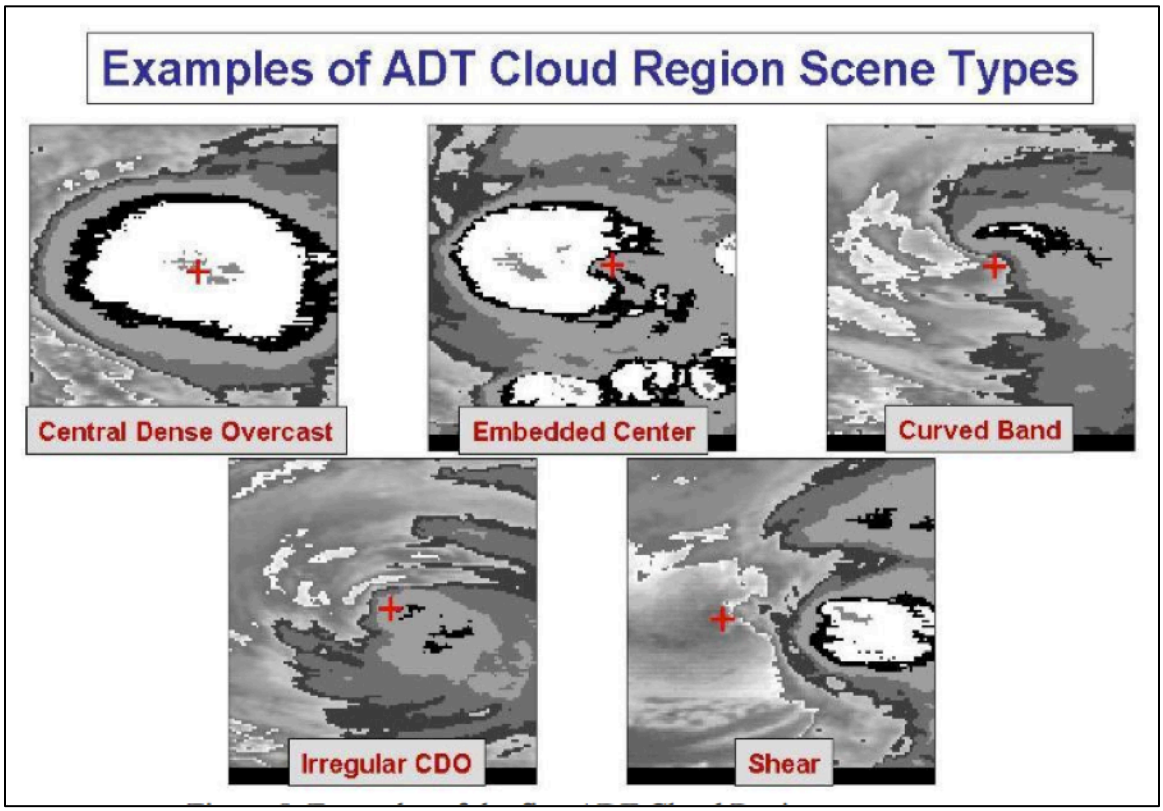

Figure 5: Examples of the five Advanced Dvorak technique cloud region scene types, including central dense overcast (CDO; top row, left), embedded center (top right, center), curved band (top row, right), irregular CDO (bottom row, left), and shear (bottom row, right). Reproduced from Olander and Velden (2013), their Figure 5.

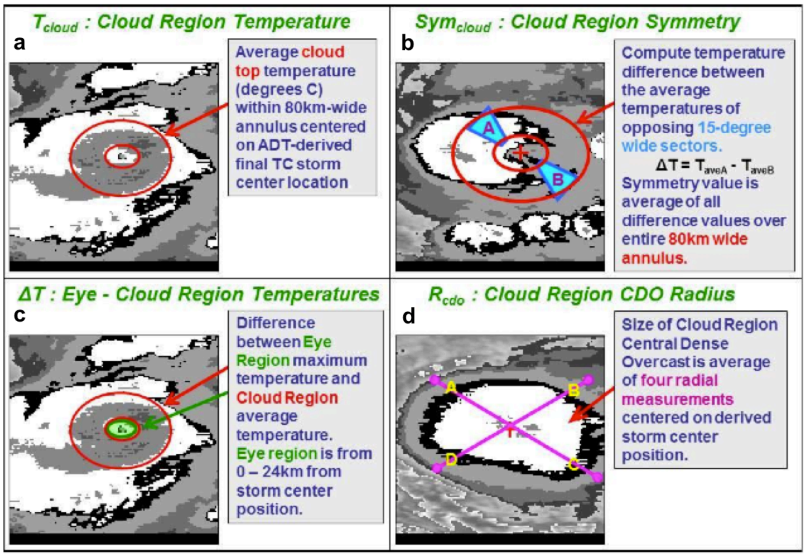

Figure 6: Images depicting the (a) T_{cloud}, (b) sym_{cloud}, (c) ΔT, and (d) R_{cdo} processes used to improve scene score and intensity estimates within ADT. Reproduced from the ADT Users' Manual, their Figure 6.

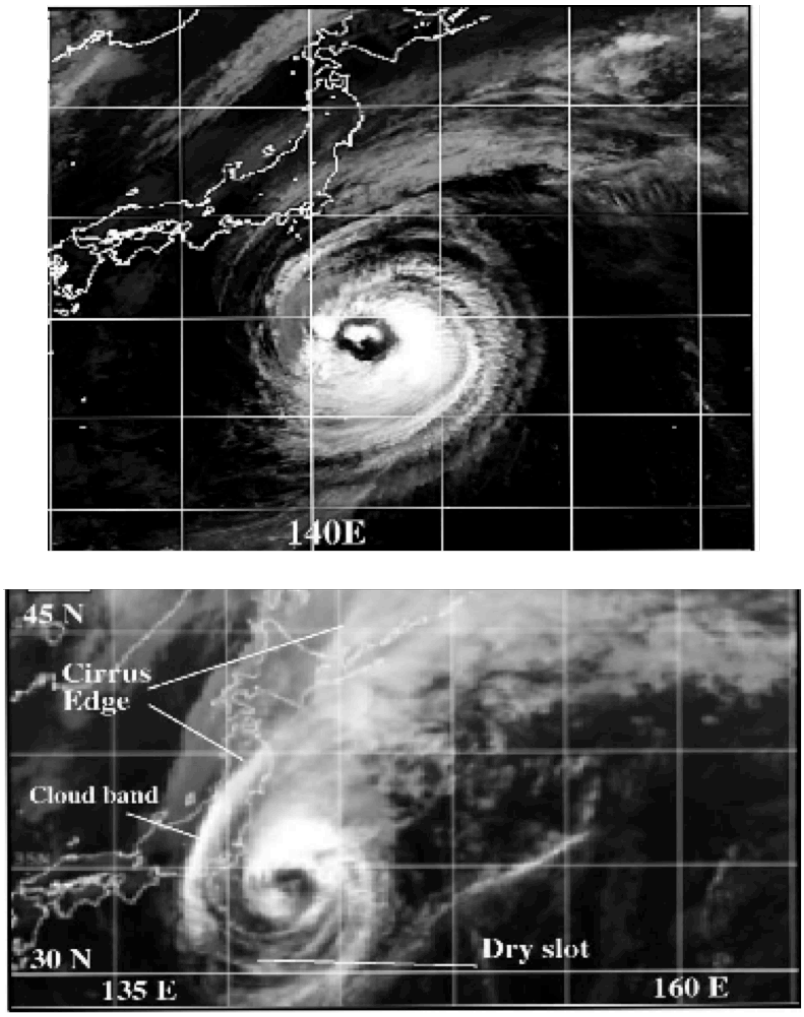

Figure 7: Geostationary Meteorological Satellite (GMS) infrared satellite imagery of western North Pacific Typhoon David at 2332 UTC 17 September 1997 (top) and 1232 UTC 18 September 1997 (bottom). The top and bottom images depicts the typhoon's cloud patterns prior to the start and during the middle of extratropical transition, respectively. Key structural characteristics at each time are labeled with white text and arrows. Reproduced from Jones et al. (2003), their Figures 12a,c.

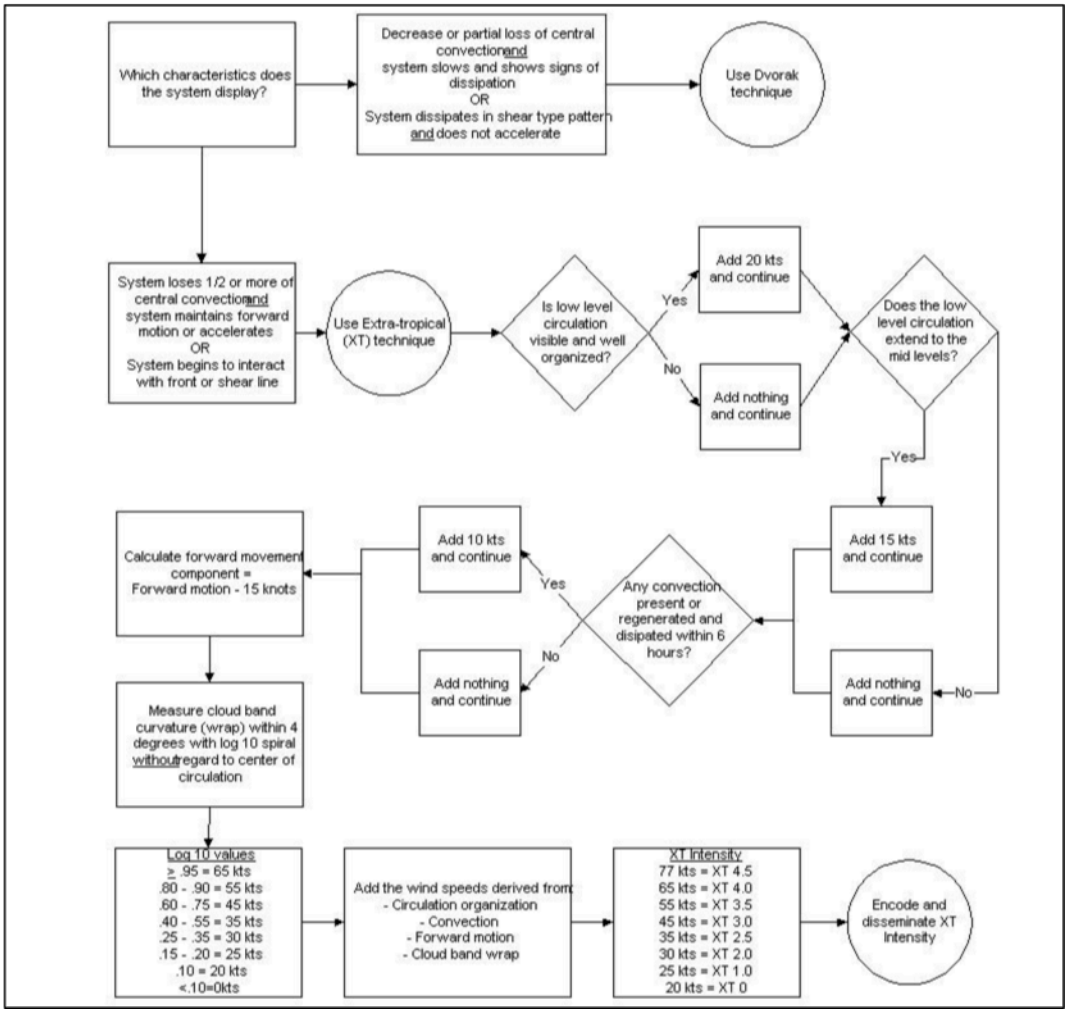

Figure 8: Flowchart utilized by the XT technique of Miller and Lander (1997) to estimate TC intensity during ET. Reproduced from Figure 6 of Miller and Lander (1997).

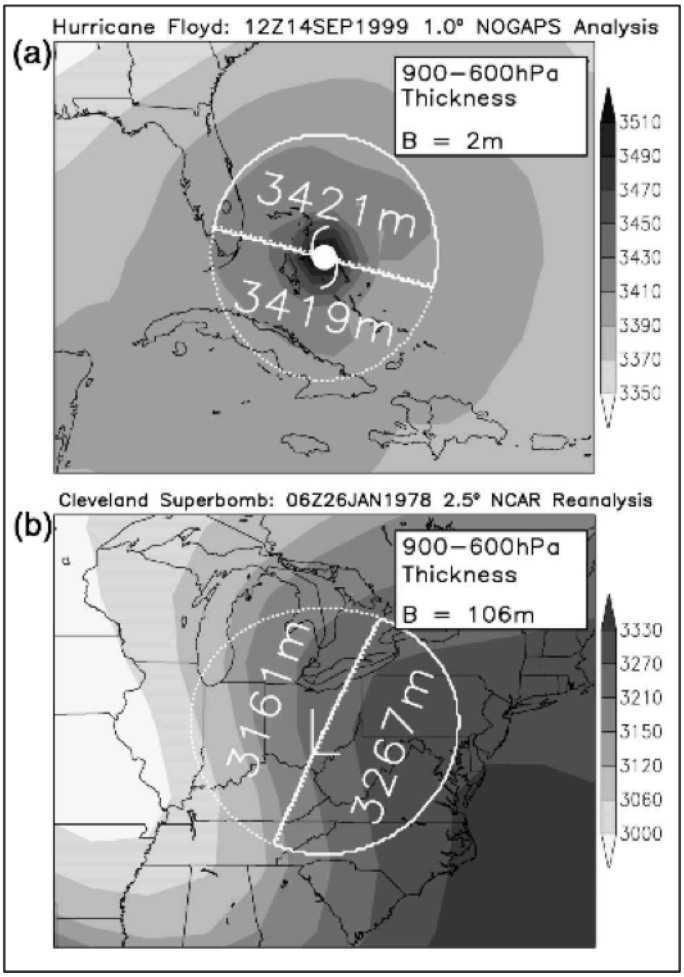

Figure 9: Example 900–600-hPa thicknesses (shaded) across a (a) thermally symmetric, or non-frontal, tropical cyclone (North Atlantic Hurricane Floyd at 1200 UTC 14 September 1999) and (b) thermally asymmetric, or frontal, extratropical cyclone ("Cleveland superbomb" at 0600 UTC 26 January 1978). The cyclone center is labeled within the 500-km-radius circle and the bisecting equator indicates direction of motion. The solid semicircle lies to the right of motion and dotted semicircle lies to the left of motion. The mean thickness for each semicircle is labeled and the thickness difference between the semicircles is listed within the inset. Panel (a) is obtained from 1° NOGAPS model operational analyses while panel (b) is obtained from 2.5° NCEP-NCAR Reanalysis. Reproduced from Hart (2003), their Figure 2.

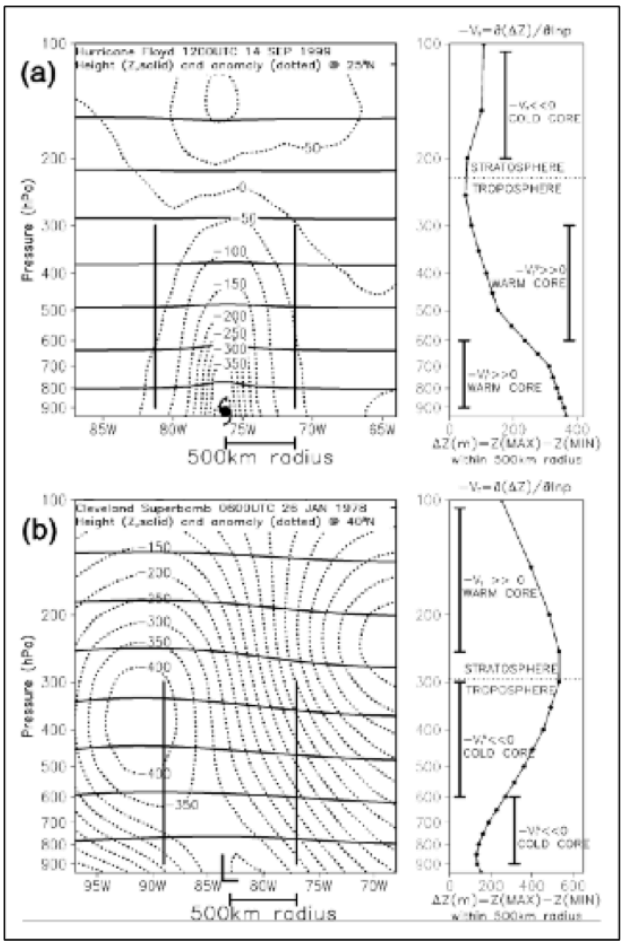

Figure 10: Derivation of parameters $-V_L^T$ (lower tropospheric thermal wind) and $-V_U^T$ (upper tropospheric thermal wind) for (a) a tropical cyclone exhibiting warm-core structure (North Atlantic Hurricane Floyd at 1200 UTC 14 September 1999) and (b) an extratropical cyclone exhibiting cold-core structure ("Cleveland superbomb" at 0600 UTC 26 January 1978). (left) Longitudinal cross section of height (Z, m; solid contour every 2000 m) and anomaly from zonal mean (dotted, m). Two vertical lines indicate the 500-km radius. (right) Height difference (ΔZ) within this radius. Cyclone phase is derived from thermal wind $[\partial(\Delta Z)/\partial \ln p]$ in two layers. $-V_L^T$ is calculated using a linear-regression fit of ΔZ between 900 and 600 hPa, while $-V_U^T$ is calculated similarly between 600 and 300 hPa. Anomaly from zonal mean (dotted on left) clearly illuminates cyclone tilt in (b). It is the tilt that leads to the correct cold-core diagnosis in (b). The data sources used to obtain each panel are as in Figure 5. Reproduced from Hart (2003), their Figure 3.

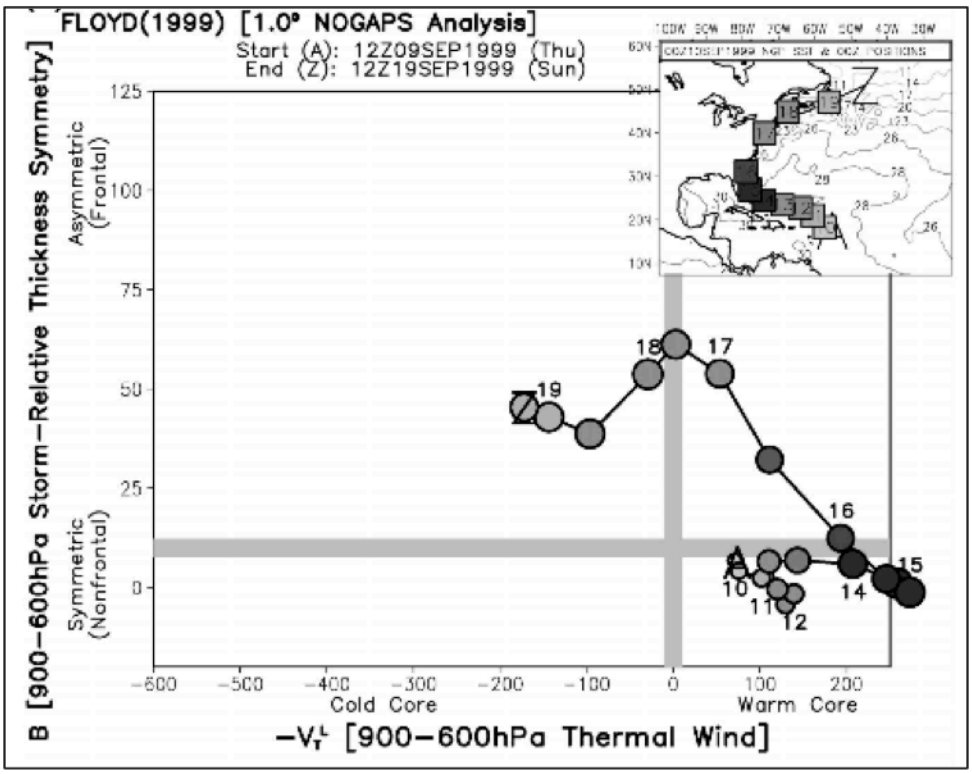

Figure 11: Cyclone phase space diagram, depicting lower tropospheric thermal wind ($-V_L^T$, horizontal axis) and lower tropospheric thermal asymmetry (B, vertical axis), for North Atlantic Hurricane Floyd between 1200 UTC 9 September 1999 and 1200 UTC 19 September 1999. Diagram obtained from 1° NOGAPS model operational analyses. The start (end) of the cyclone's trajectory through the phase space is depicted by an A (a Z). The relative intensity of the cyclone, as assessed utilizing minimum sea level pressure, is given by the color shading of each circle, with darker colors denoting a more intense cyclone. The relative size of the cyclone's 925 hPa gale-force (>17 m s^{-1}) wind field is given by the size of the color-shaded circle. Reproduced from Hart (2003), their Figure 6a.

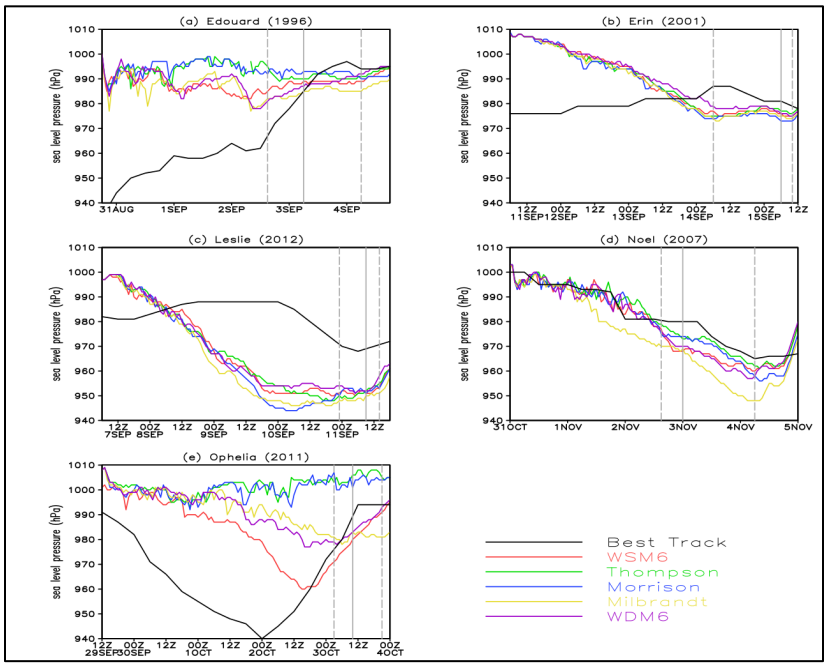

Figure 12: Best track and model-derived ("truth") pressure (hPa) intensity values for (a) Edouard, (b) Erin, (c) Leslie, (d) Noel, and (e) Ophelia. Vertical left and right dashed lines represent average ET start and ET end times respectively.

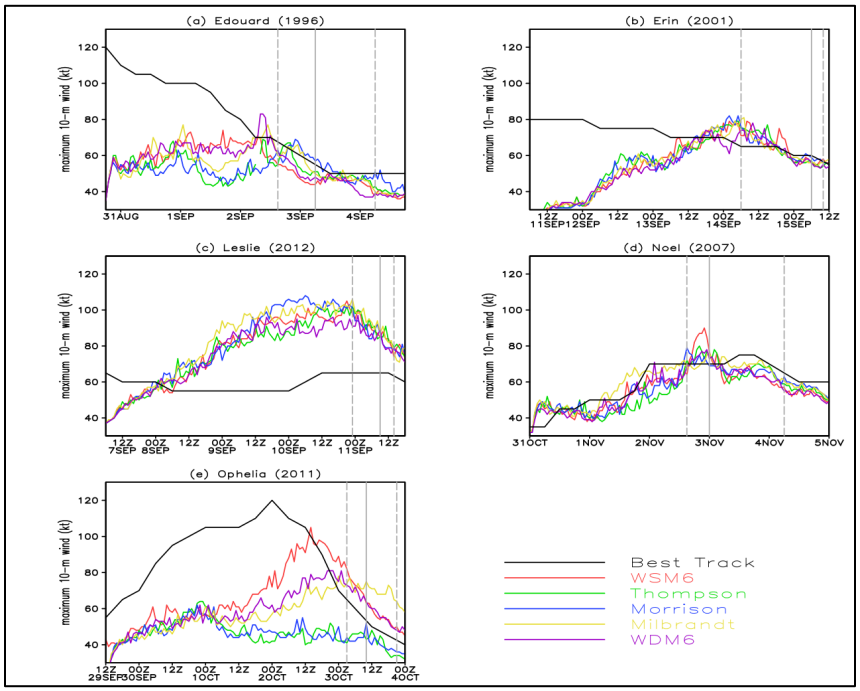

Figure 13: Best track and model-derived ("truth") wind (kt) intensity values for (a) Edouard, (b) Erin, (c) Leslie, (d) Noel, (e) Ophelia. Vertical left and right dashed lines represent average ET start and ET end times respectively.

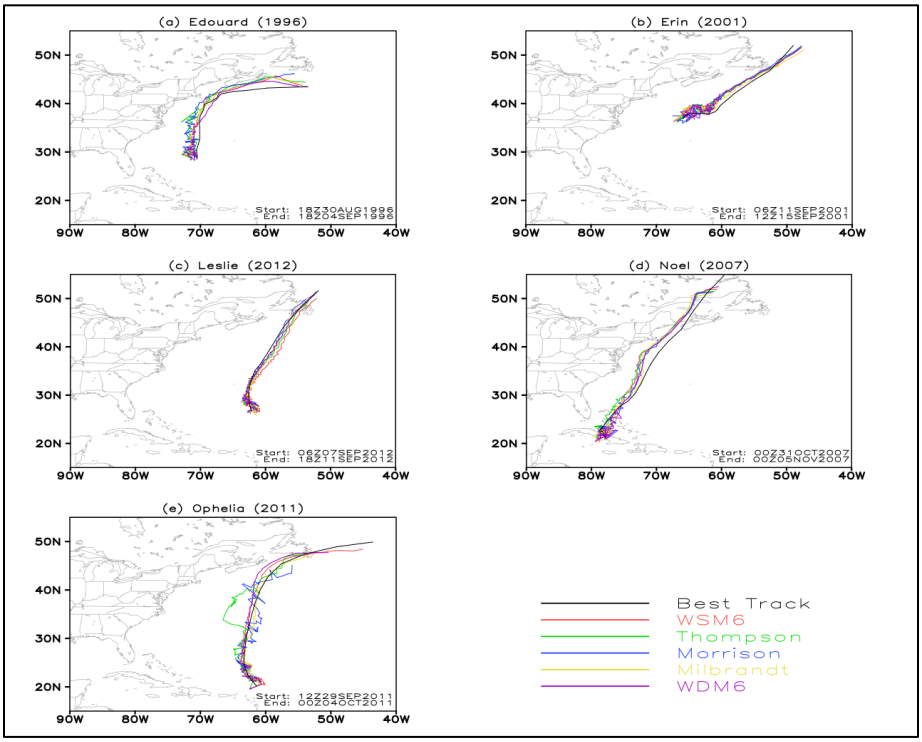

Figure 14: Best Track and Model-simulation storm track for the five-day model duration for Edouard (a), Erin (b), Leslie (c), Noel(d), and Ophelia (e).

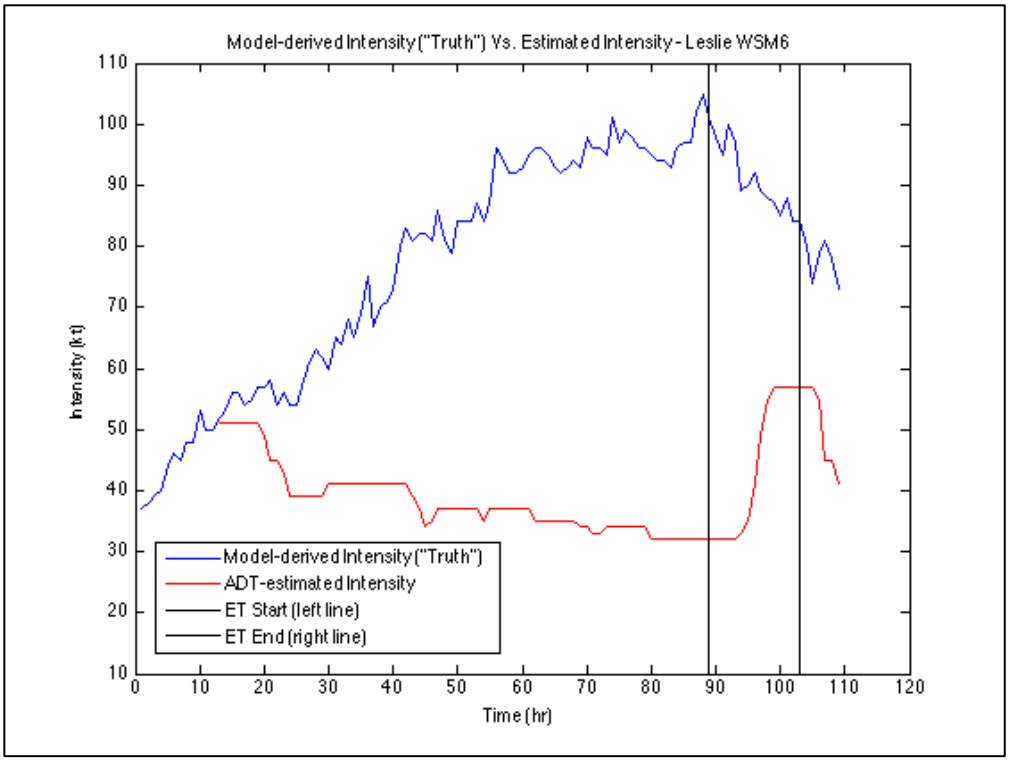

Figure 15: Representative display of model-derived intensity, or "truth" (kt, blue line), and ADT-estimated (from synthetic satellite imagery) intensity (kt, red line), as obtained from the WSM6 microphysical scheme-based WRF-ARW simulation of Hurricane Leslie (2012). The *x*-axis depicts the forecast hour of the numerical simulation. The cyclone phase space-determined start and end of ET are given by the leftmost and rightmost black vertical lines, respectively.

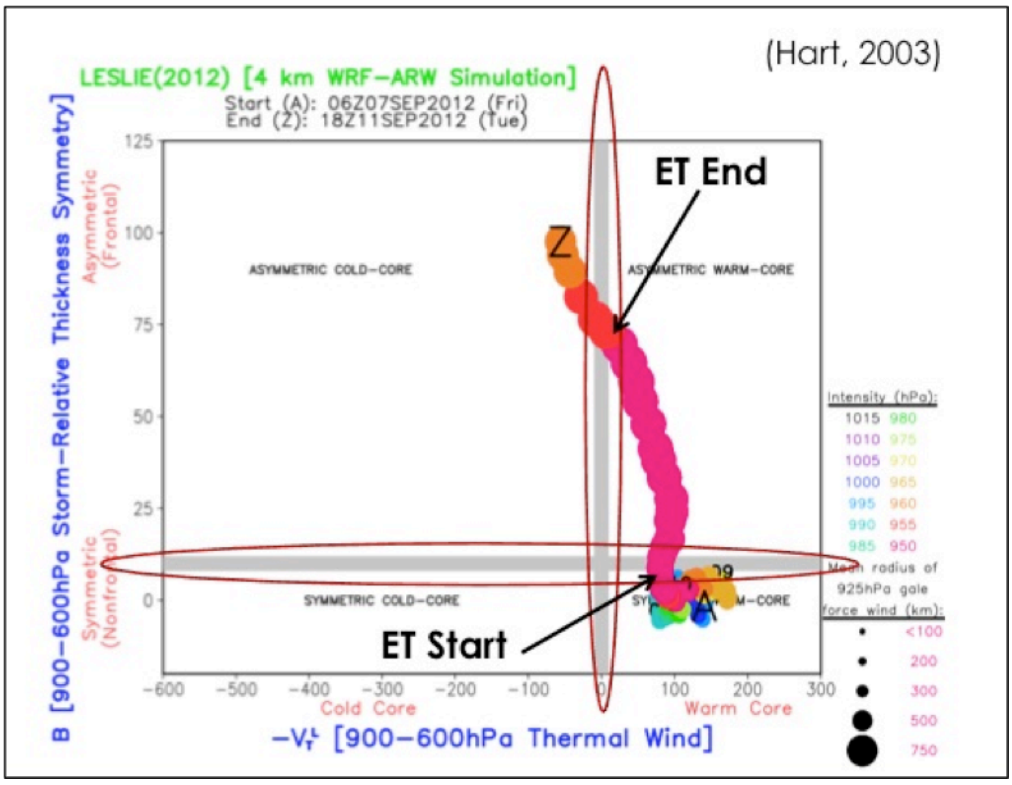

Figure 16: Cyclone phase space image, interpreted in the same fashion as Figure 8 above, obtained from the WRF-ARW model simulation of Hurricane Leslie (2012) utilizing the WSM6 microphysical scheme with the B = 10 m ET start and $-V_T^L < 0$ ET end thresholds explicitly annotated

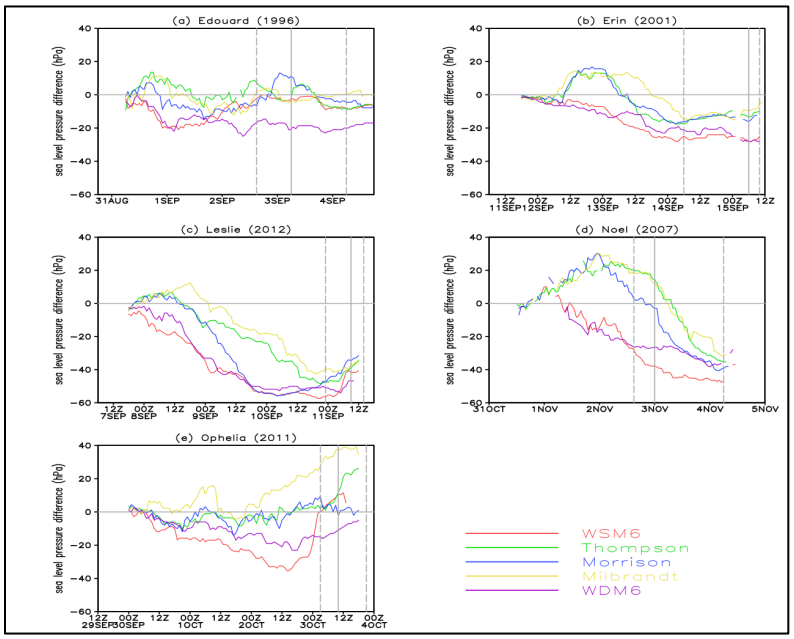

Figure 17: Model-Derived ("Truth") minus ADT-Estimated Pressure (hPa) Error for similar storms with varying microphysical schemes. The left and right dashed lines correspond to the average ET start and ET end for the storm over the five scheme respectively, with the solid vertical line corresponding to the National Hurricane Center (NHC) best track end time.

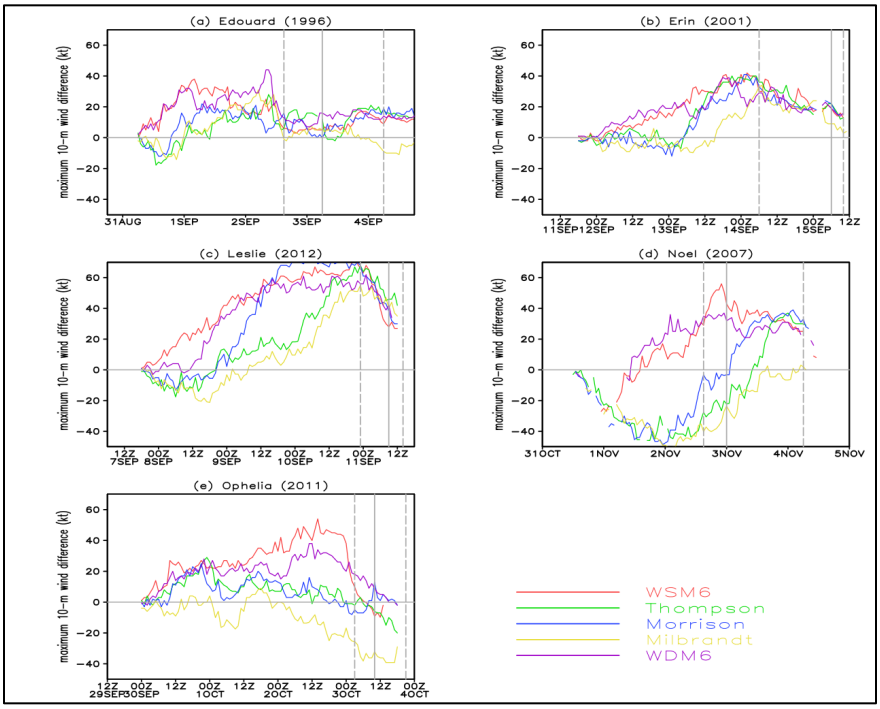

Figure 18: Model-Derived ("Truth") minus ADT-Estimated Wind (kt) Error for similar storms with varying microphysical schemes. The left and right dashed lines correspond to the average ET start and ET end for the storm over the five scheme respectively, with the solid vertical line corresponding to the National Hurricane Center (NHC) best track end time.

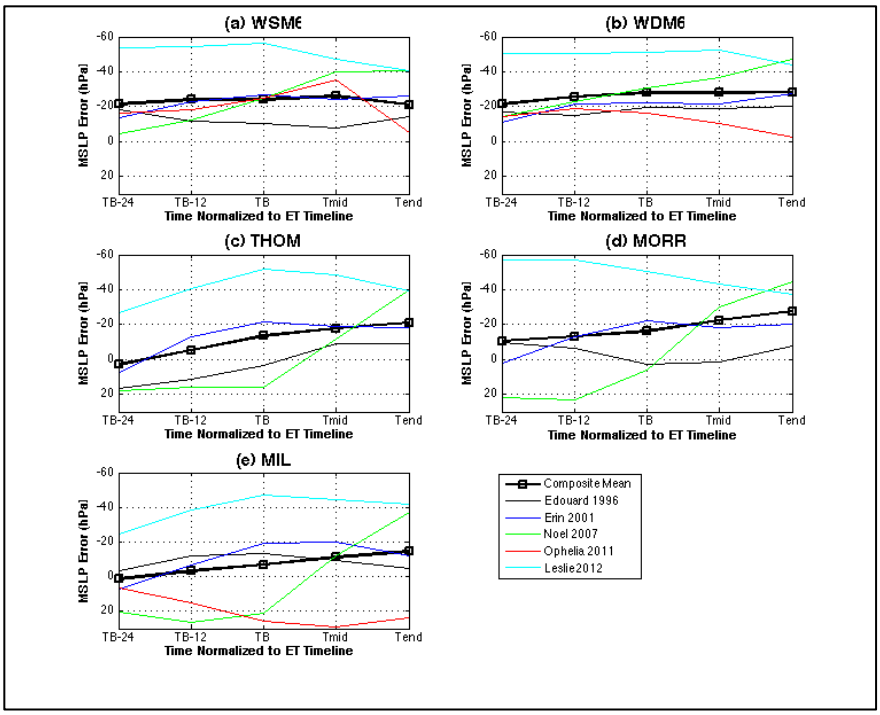

Figure 19: Model-Derived ("Truth") minus ADT-Estimated Pressure (hPa) Error for all storms within their respective microphysical scheme, normalized to the ET timeline.

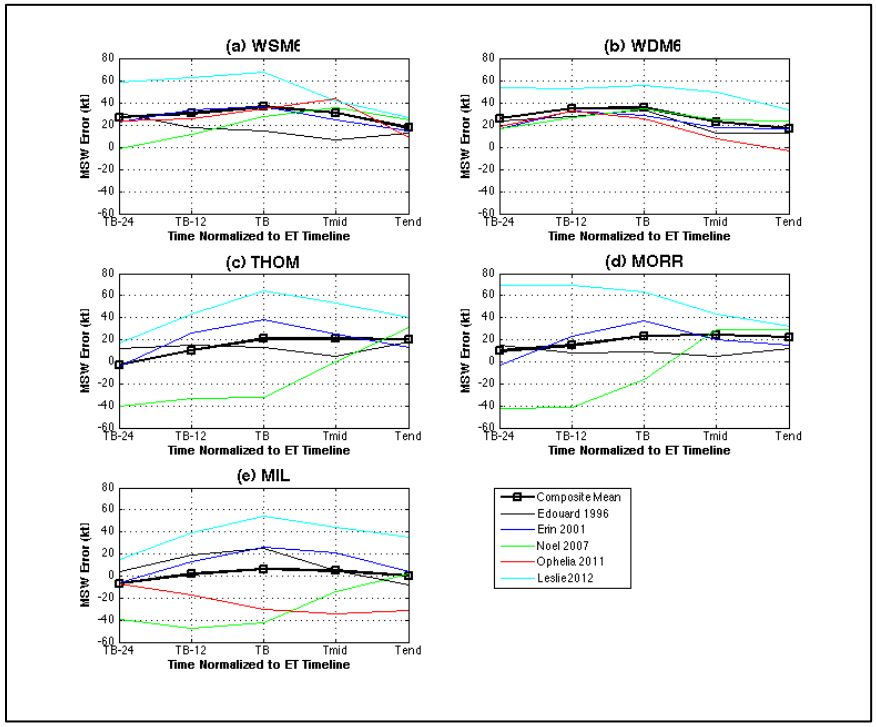

Figure 20: Model-Derived ("Truth") minus ADT-Estimated Wind (kt) Error for all storms within their respective microphysical scheme, normalized to the ET timeline.

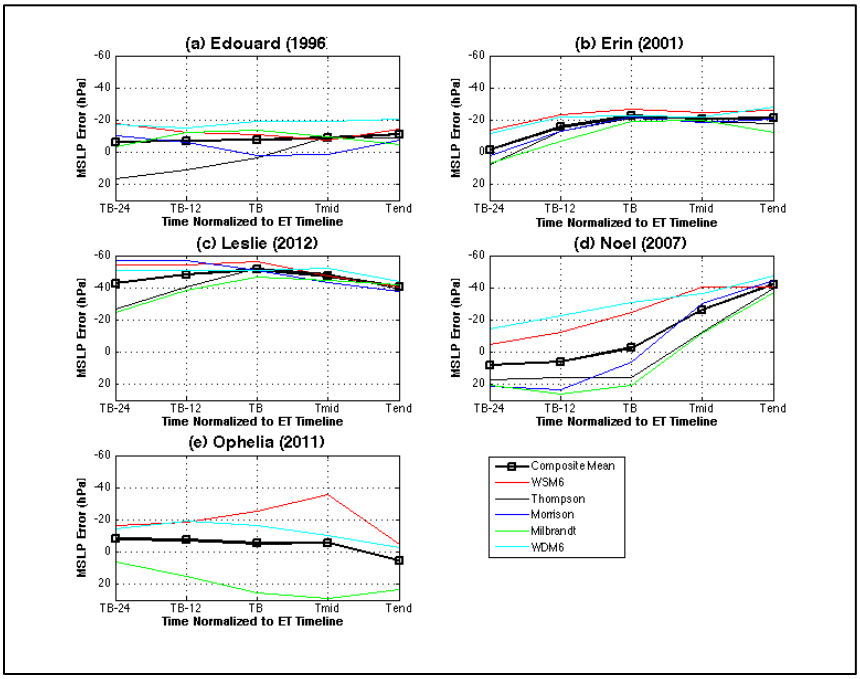

Figure 21: Model-Derived ("Truth") minus ADT-Estimated Pressure (hPa) Error for similar storms with varying microphysical scheme, normalized to the ET timeline.

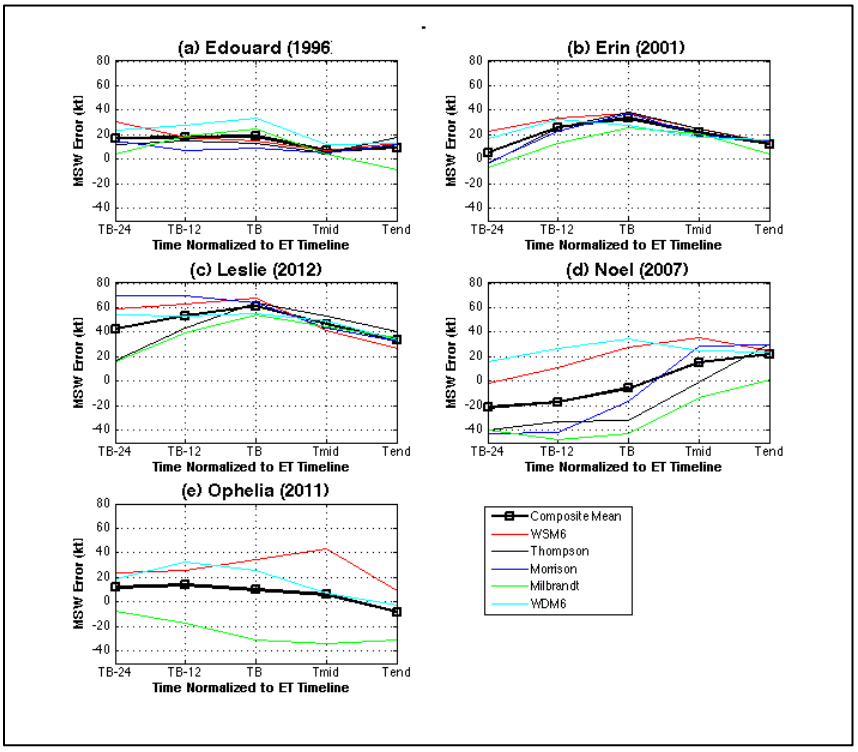

Figure 22: Model-Derived ("Truth") minus ADT-Estimated Wind (kt) Error for similar storms with varying microphysical scheme, normalized to the ET timeline.

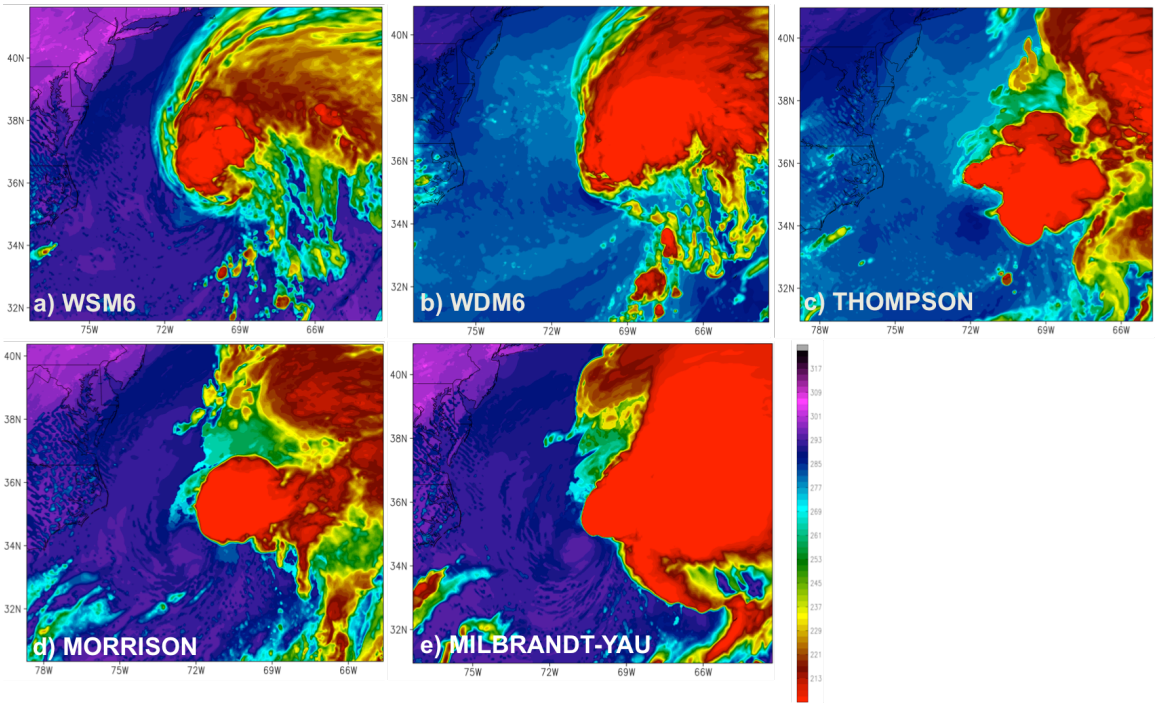

Figure 23: SSI for Edouard, taken on 09/01 18Z or 48 hours into the simulation. A visible eye is not seen at anytime in Edouard as it displays upper level clouds (denoted by cold cloud top temperatures) both over the storm center and northeast of storm center.

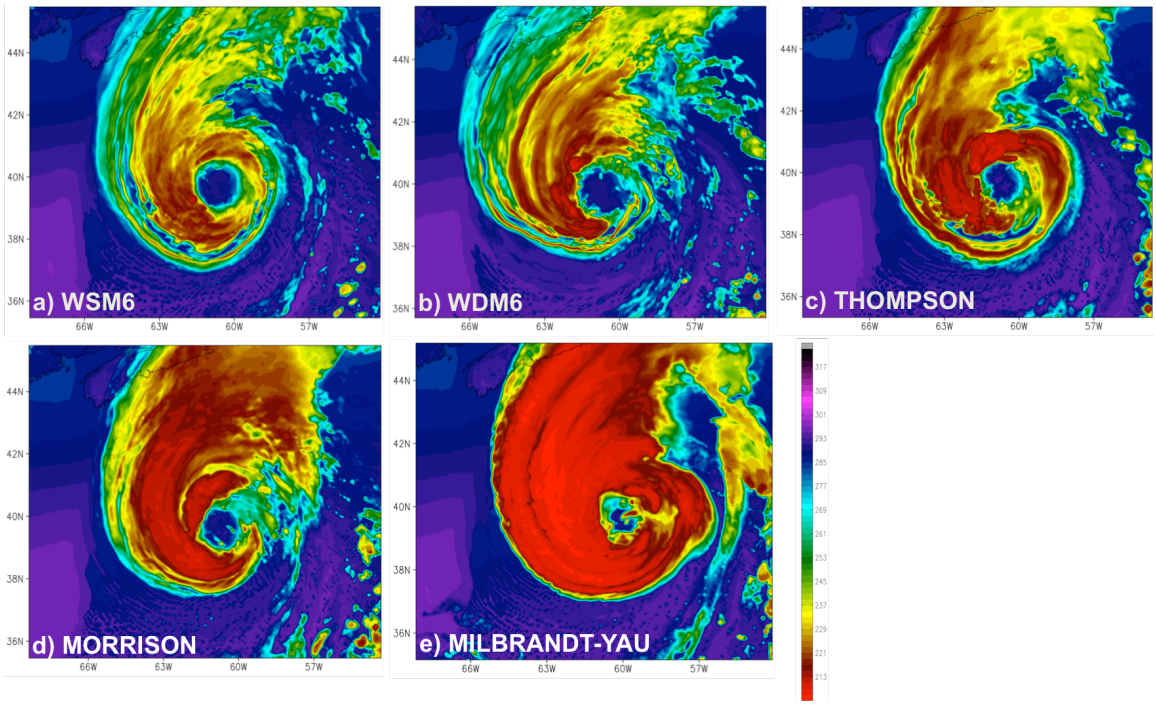

Figure 24: SSI for Erin on 09/13 20Z or 61 hours into the simulation. Erin displays a discernable eye leading into ET start, where it is quickly eroded by cold, descending air from the northwest of storm center (not pictured).

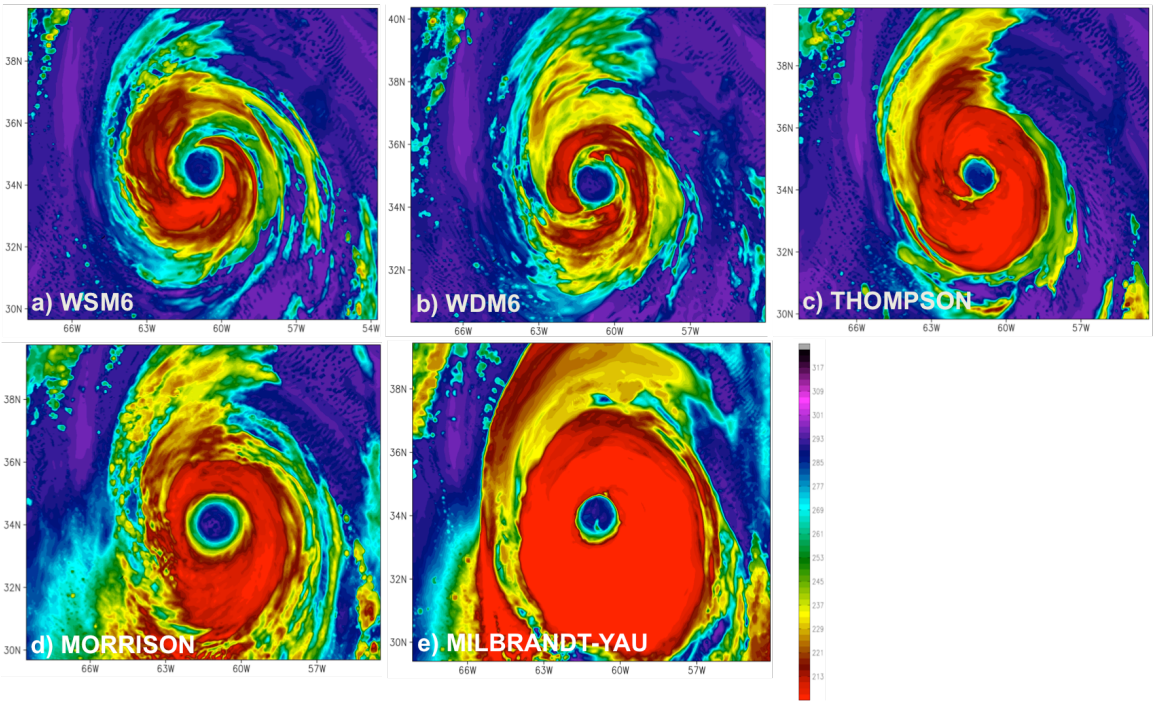

Figure 25: SSI for Leslie at 09/10 06Z or 72 hours into the simulation. A discernable large eye is seen leading into the start of ET.

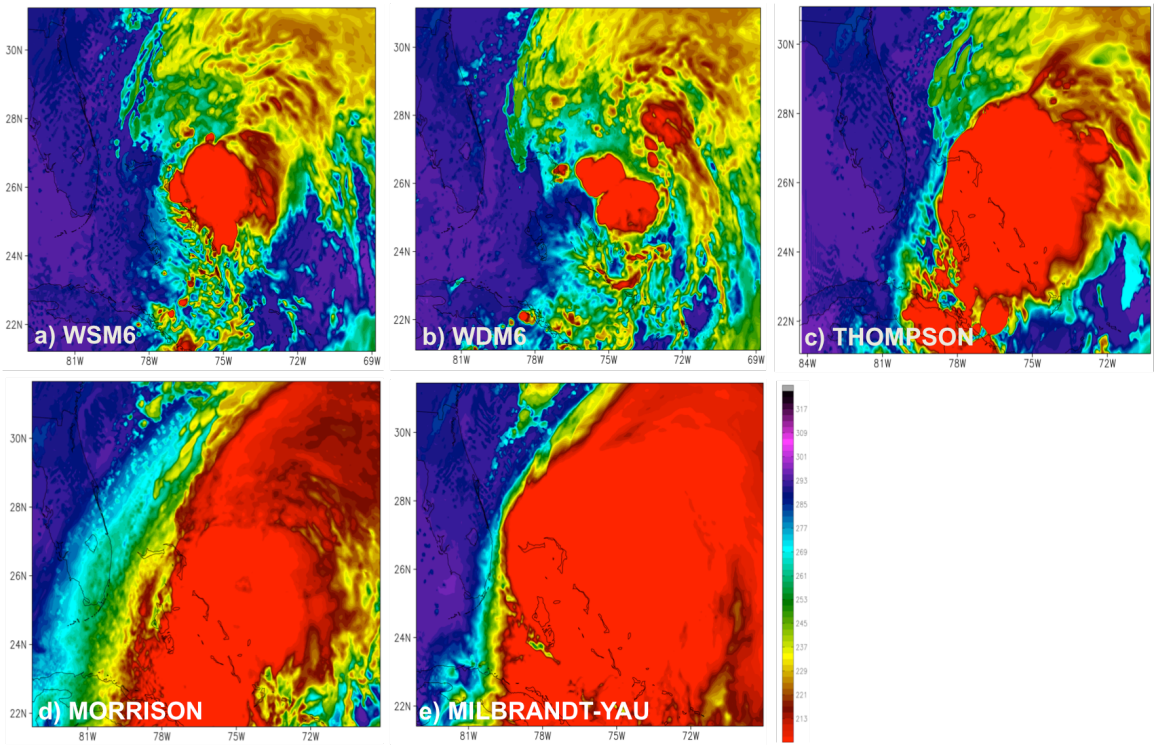

Figure 26: SSI for Noel at 11/02 00Z or 48 hours into the simulation. An eye is not seen throughout any part of the simulation. The Thompson, Morrison, and Milbrandt cases display an excess amount of upper-level clouds to the north, south, and east of the storm.

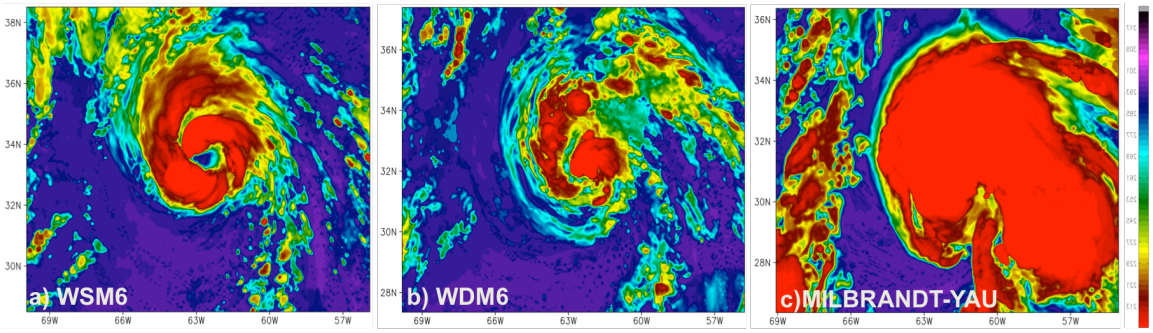

Figure 27: SSI for Ophelia on 10/02 06Z or 66 hours into the simulation. The WSM6 case shows a discernable eye leading up to ET start, while the WDM6 and Milbrandt schemes exhibit cloud over storm center, with the spatial extent of clouds being much greater in the Milbrandt scheme.

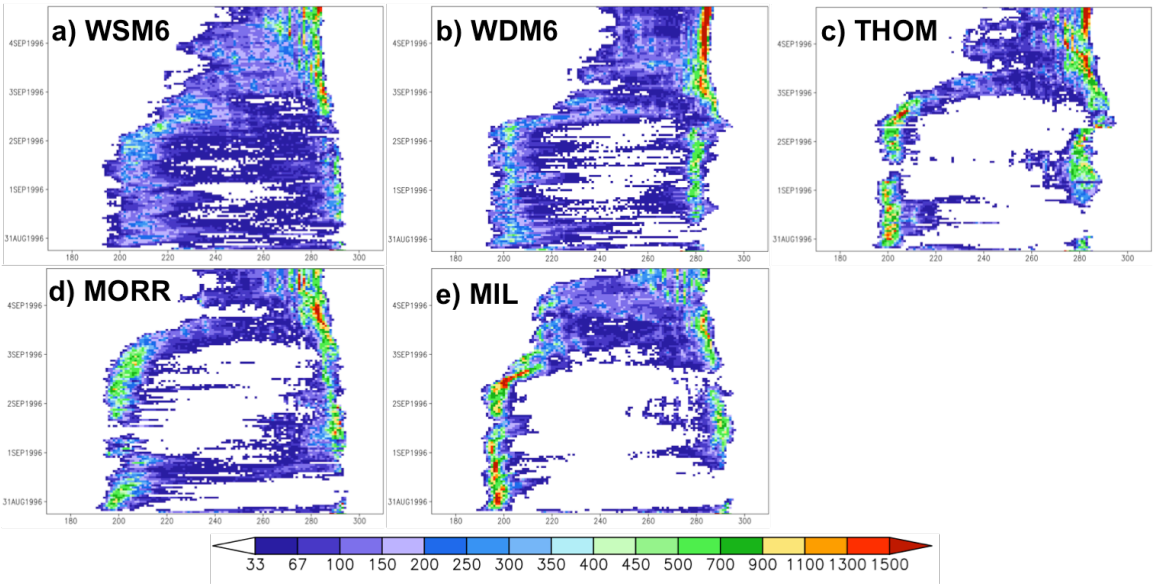

Figure 28: Hovmöller-style histograms for Edouard (1996), displaying number of grid points correlated to temperature values within 200 km from model-derived storm center. Warmer colors indicate a larger extent of grid points for its respective temperatures along the x-axis, with the y-axis depicting time.

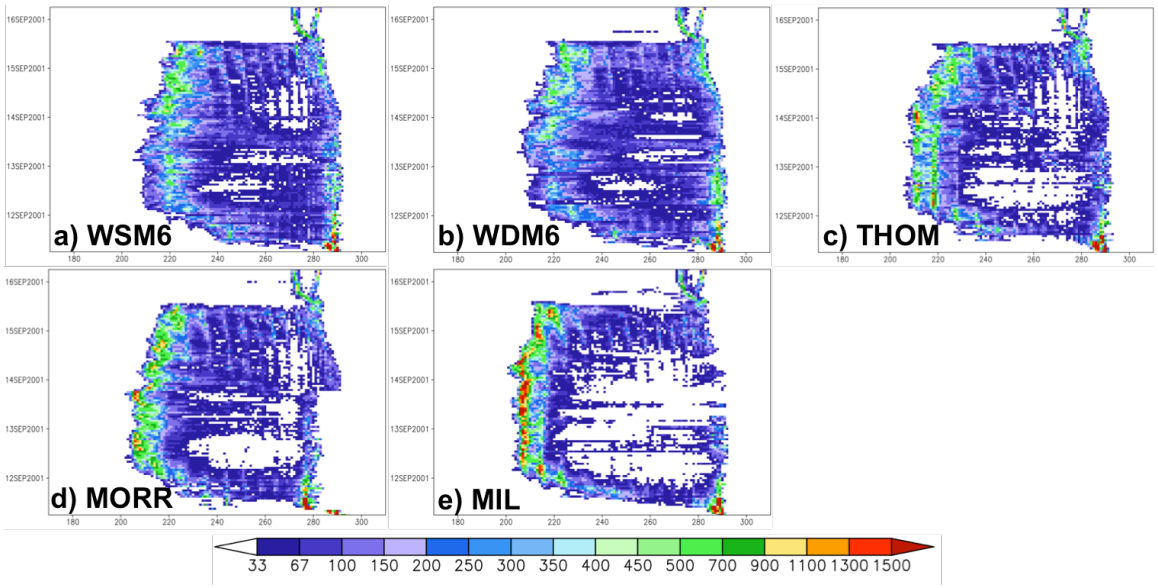

Figure 29: Same as Figure 25, for Erin (2001).

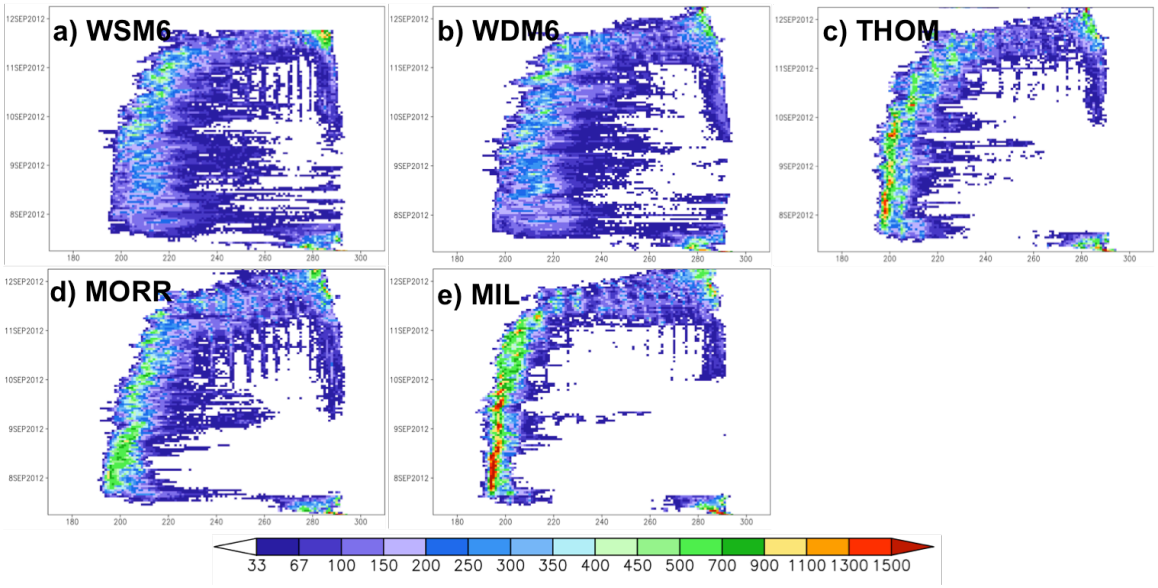

Figure 30: Same as Figure 25, for Leslie (2012)

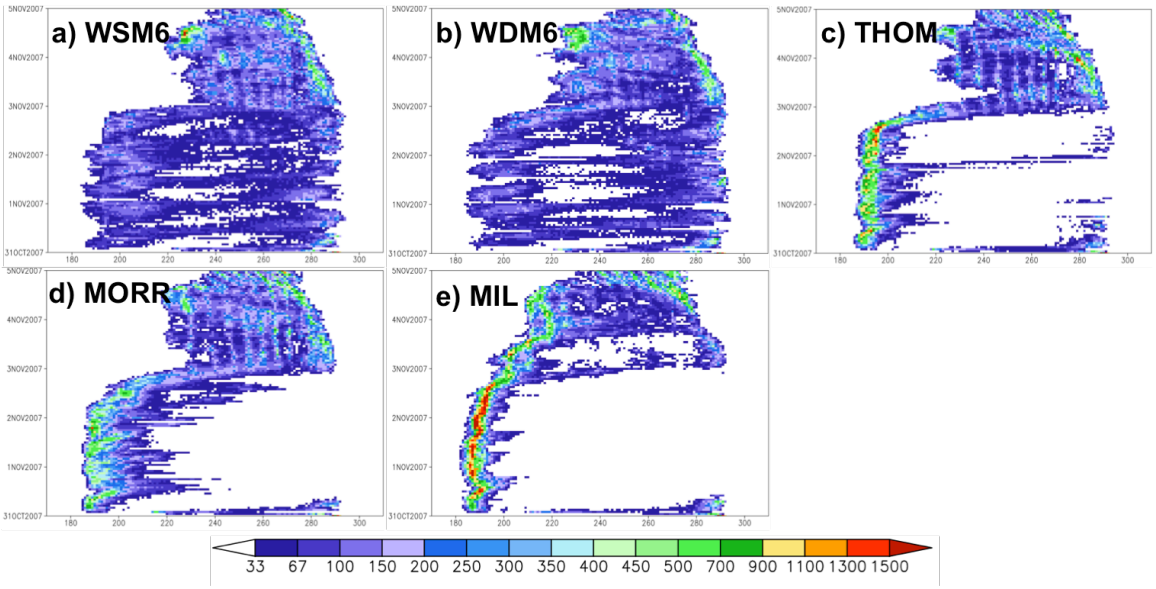

Figure 31: Same as Figure 25, for Noel (2007).

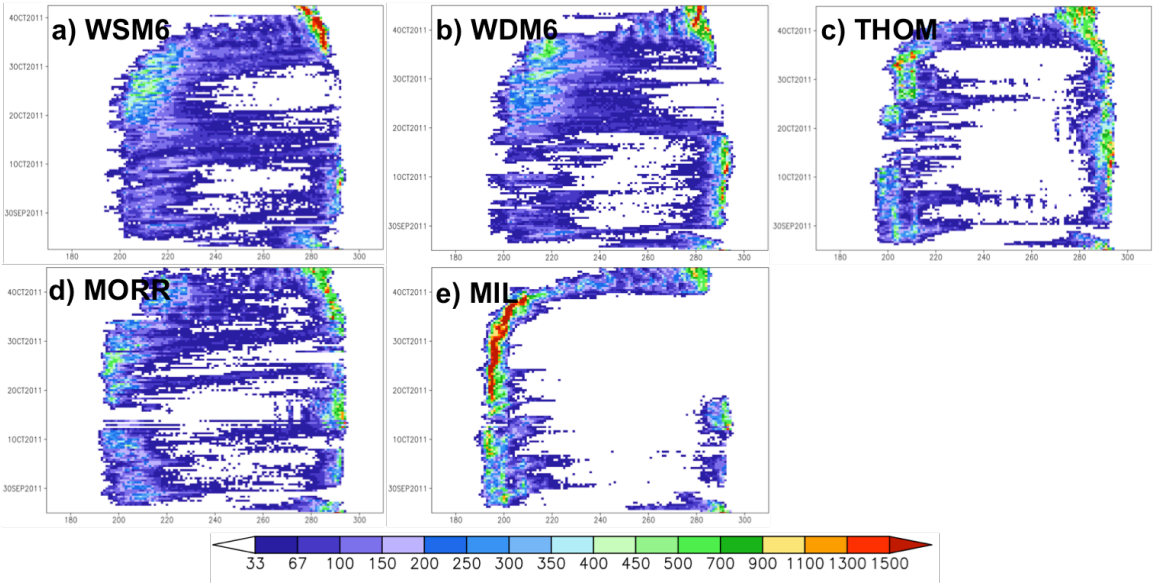

Figure 32: Same as Figure 25, for Ophelia (2011).

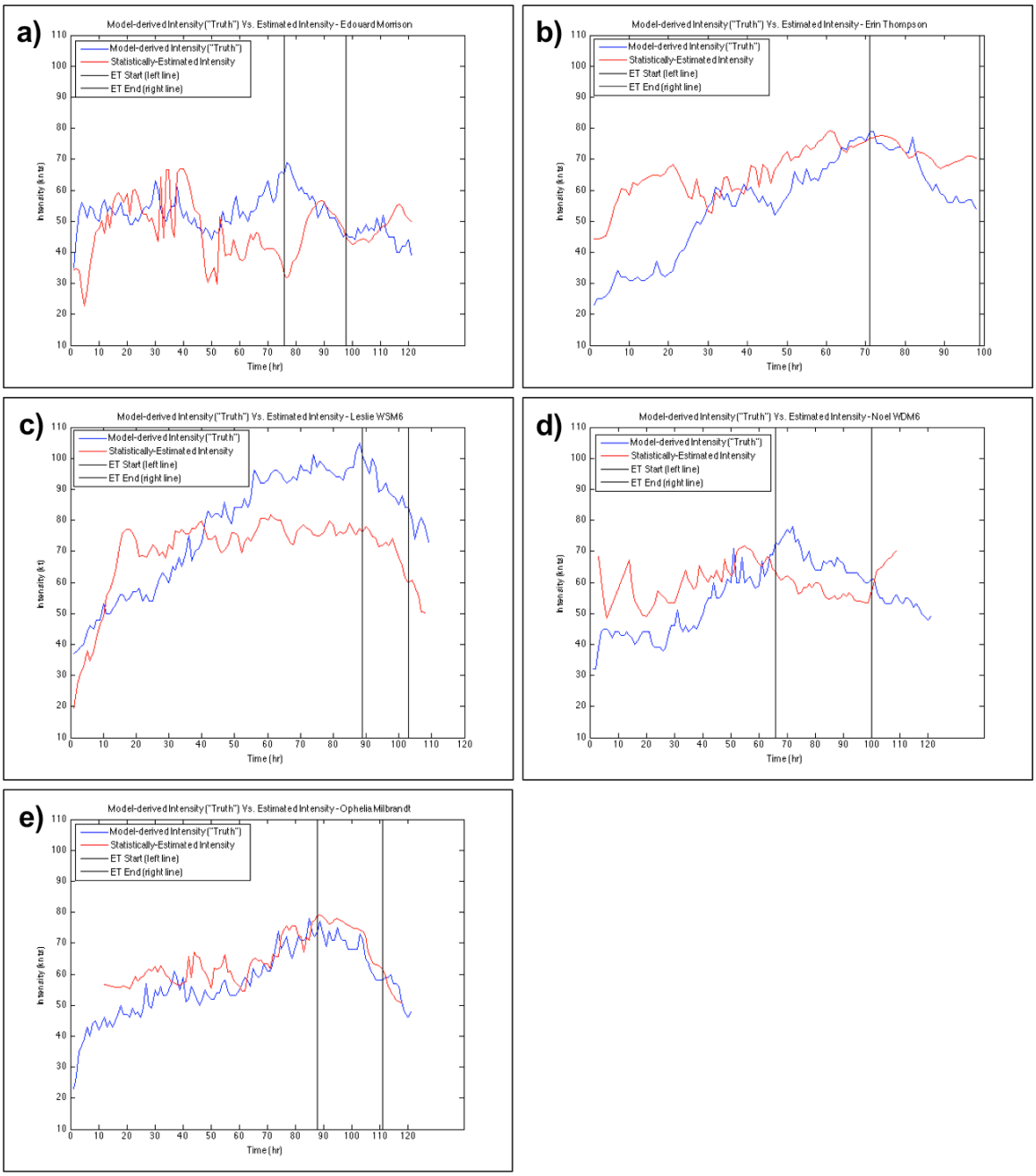

Figure 33: Model-Derived ("truth") Vs. Statistically-Estimated Wind Intensity (kt) for (a) Edouard Morrison, (b) Erin Thompson, (c) Leslie WSM6, (d) Noel WDM6, and (e) Ophelia Milbrandt.

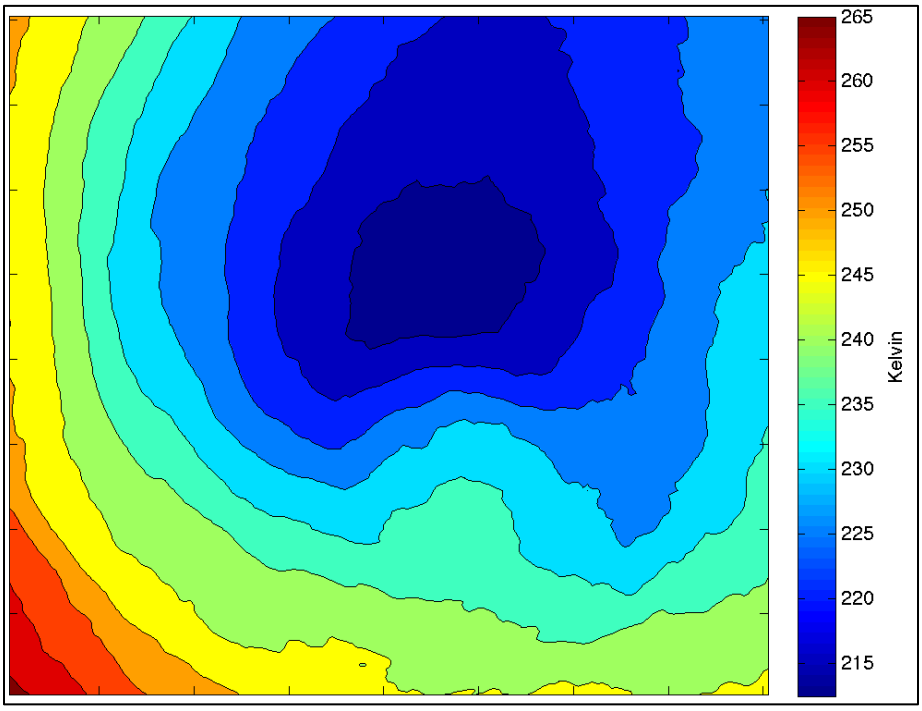

Figure 34: Composite mean storm cloud top temperatures composed of Edouard, Erin, Leslie, and Noel (Milbrandt) on an 648 by 648 km grid, centered on model-derived storm center.

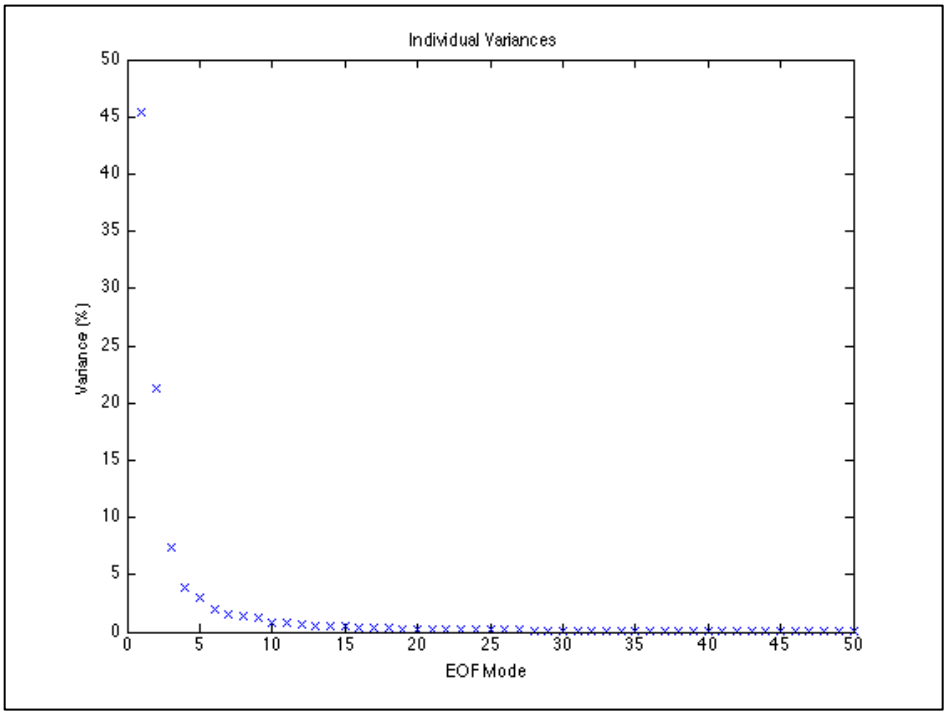

Figure 35: Variance associated with leading EOF Modes for the training dataset. The first four leading EOF modes account for 78% of the total variance and are used as predictors for deriving estimated storm intensity.

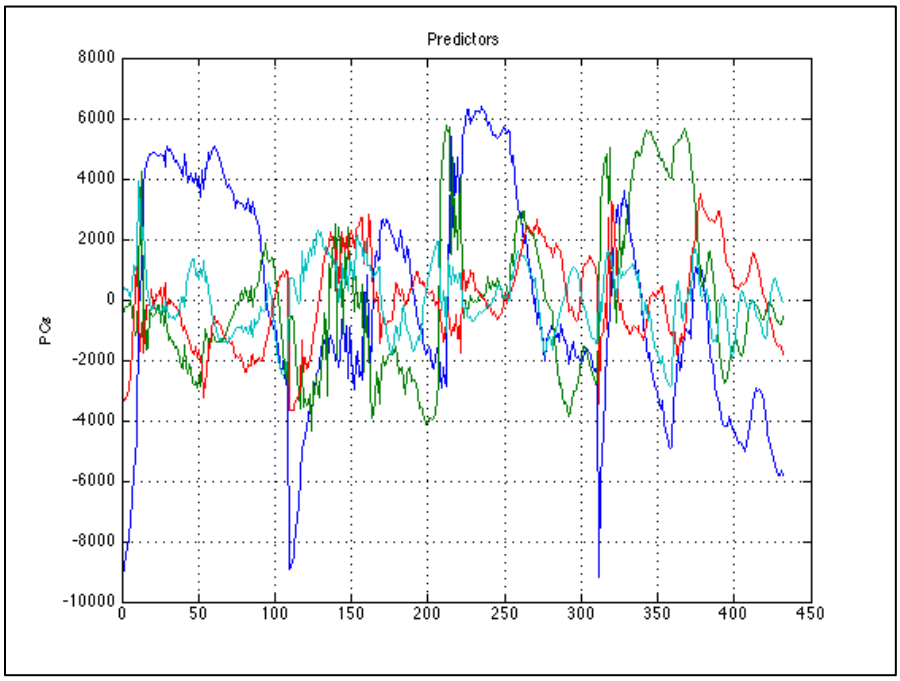

Figure 36: Predictors (first four leading PCs of the training dataset) used to determine Coefficients of equation (6), using Multiple Linear Regression

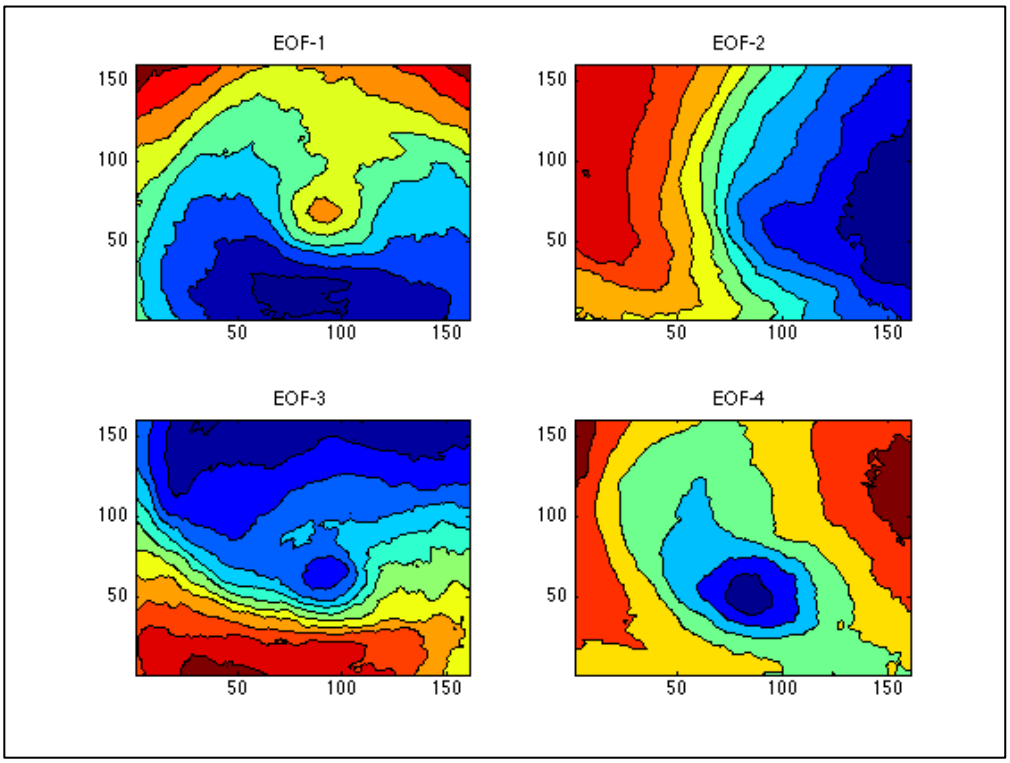

Figure 37: Four leading spatial patterns derived from the training dataset (Edouard, Erin, Leslie, and Noel -- Milbrandt), which are projected onto storm anomalies of the last storm not used in the training data (Ophelia – Milbrandt), to derive estimated storm intensities.

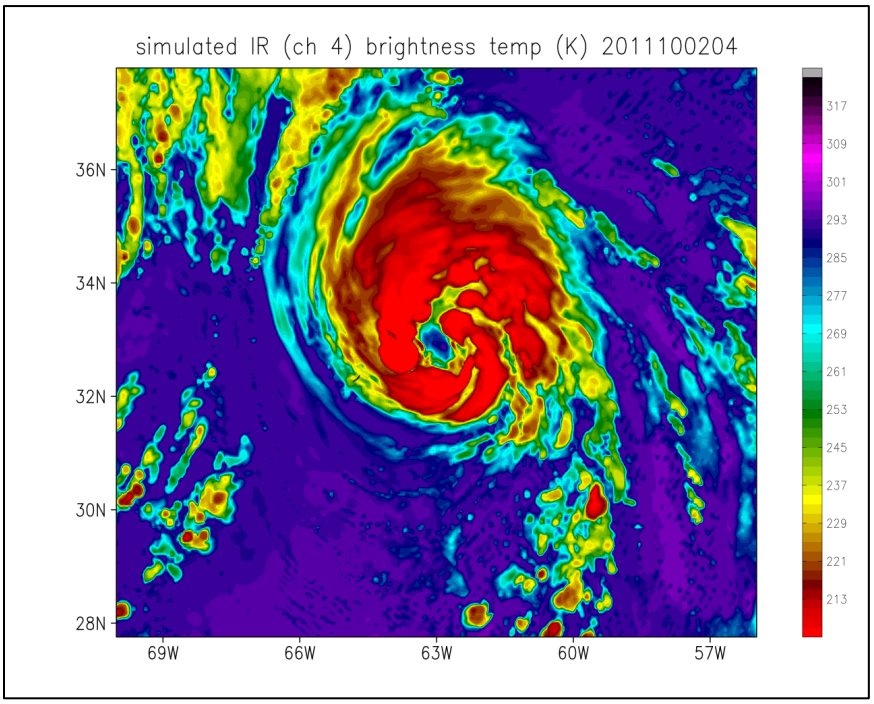

Figure 38: SSI of Hurricane Ophelia at 10/02 04Z. Despite a clearly visible eye, the shear scene type was issued for this hour.

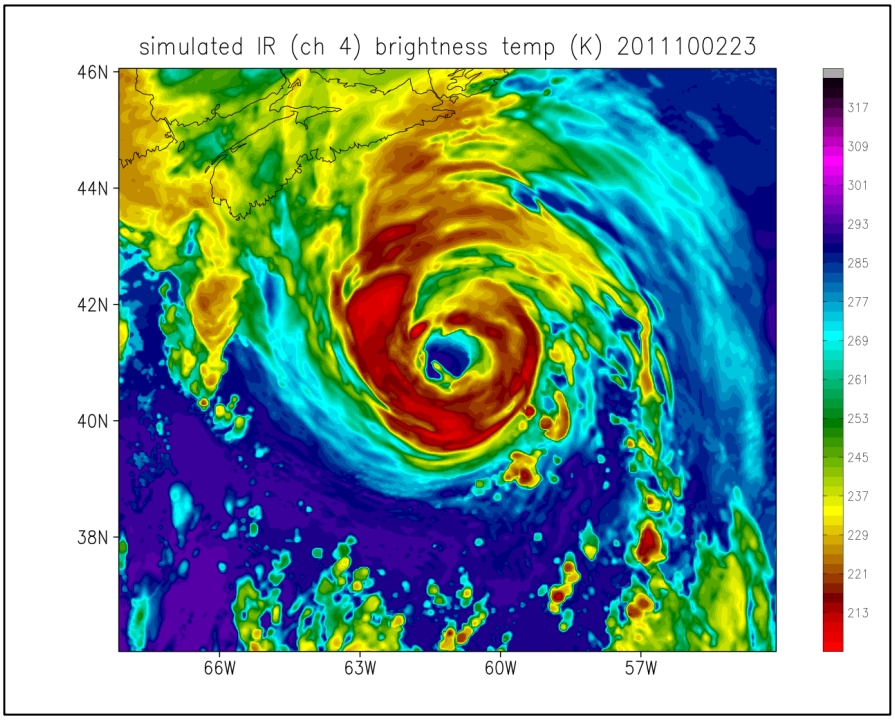

Figure 39: SSI of Hurricane Ophelia at 10/02 23Z. The eye scene was accurately captured at this time, most likely to a slightly more consistent uniform temperatures surrounding the eye, relative the Figure 37.

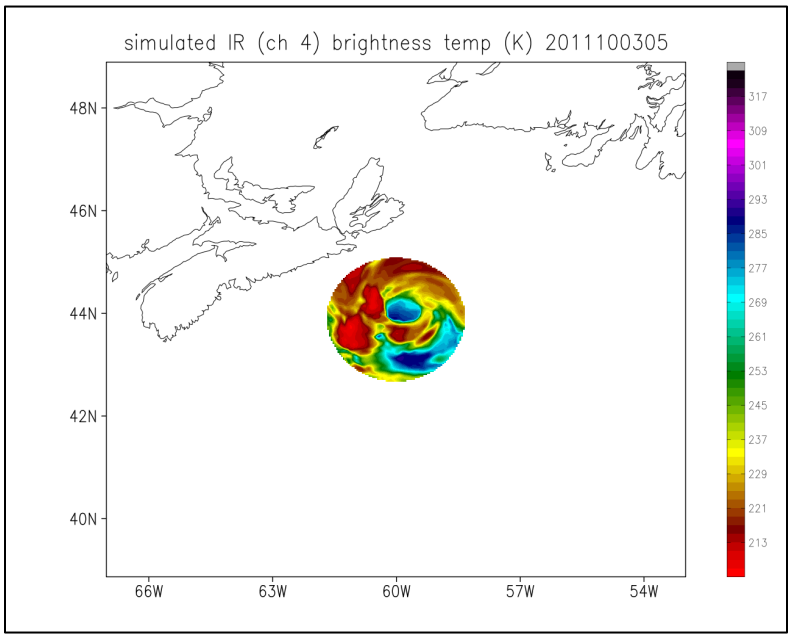

Figure 40: 136 km circle surrounding the storm center used to derive scene score for Ophelia (WSM6) on 10/03 05Z. The scene type for this image was labeled as "eye".

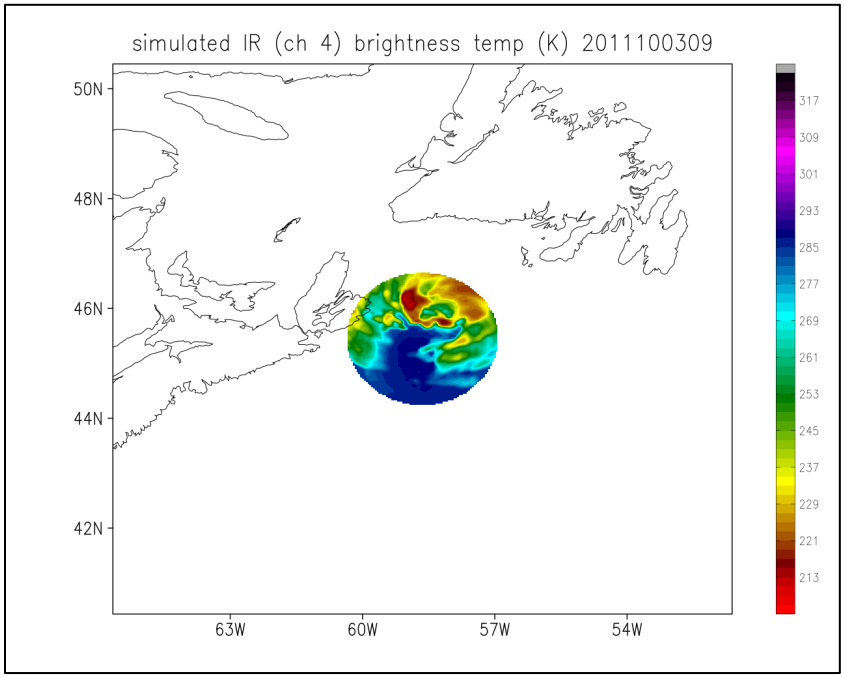

Figure 41: Ophelia (WSM6) on 10/03 09, four hours from Figure 39. The process of ET rapidly degrades the eye, as cold, descending air wraps around from the northeast, resulting in a shift from the eye scene type to shear scene type, and consequently resulting in a rapid weakening in ADT-estimates.

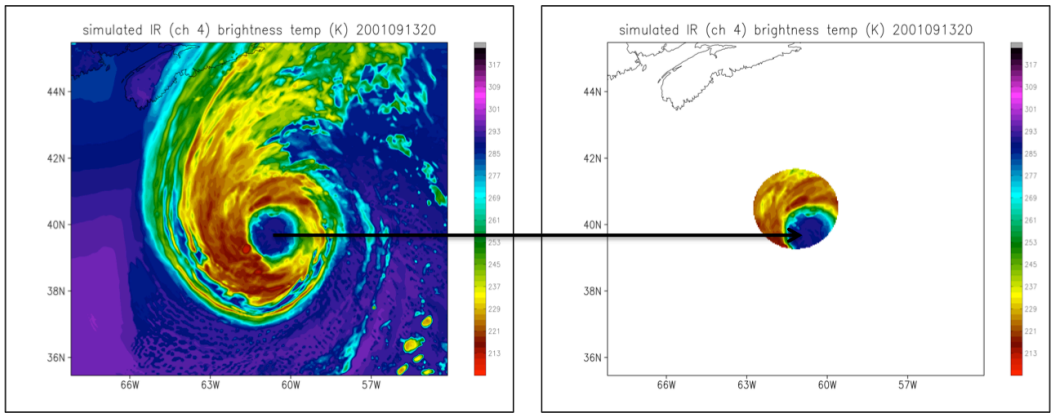

Figure 42: Erin (WSM6) at 09/13 20Z (left), with the 136km search radius ADT employs from implemented storm center (right). This illustrates how an incorrectly placed storm center can influence scene types issued by ADT. What looks to be a probably case for an eye scene type is incorrectly labeled as a curved band due to the limited vision ADT had on the storm.

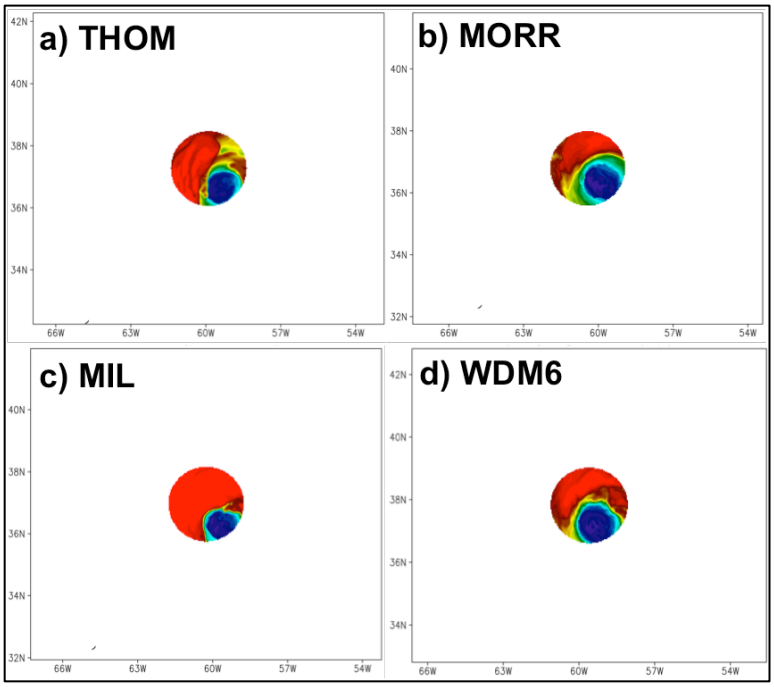

Figure 43: 136km radius centered over model-derived storm center for Leslie at 09/10 17Z for. Storm center was incorrectly placed to the northwest of the eye, resulting in potential erroneous scene types at this time

LIST OF REFERENCES

Aldinger, W. T., and W. Stapler, 1998: 1998 Annual Tropical Cyclone Report. [Available online at http://www.dtic.mil/dtic/tr/fulltext/u2/a399580.pdf.]

Avila, L. A., and S. R. Stewart, 2013: Atlantic hurricane season of 2011. *Mon. Wea. Rev.*, **141**, 2577–2596.

Beven, J. L., S. R. Stewart, M. B. Lawrence, L. A. Avila, J. L. Franklin, and R. J. Pasch, 2003: ANNUAL SUMMARY: Atlantic hurricane season of 2001. *Mon. Wea. Rev.*, **131**, 1454–1484.

Bikos, D., and coauthors, 2012: Synthetic satellite imagery for real-time high resolution model evaluation. *Wea. Forecasting*, **27**, 784–795.

Blake, E. S., T. B. Kimberlain, R. J. Berg, J. P. Cangialosi, and J. L. Beven, 2013: Tropical cyclone report: Hurricane Sandy. [Available online at http://www.nhc.noaa.gov/data/tcr/AL182012_Sandy.pdf.]

Brennan, M. J., R. D. Knabb, M. Mainelli, and T. B. Kimberlain, 2009: Atlantic hurricane season of 2007. *Mon. Wea. Rev.*, **137**, 4061–4088

Brown, D. B., and J. L. Franklin, 2002: Accuracy of pressure-wind relationships and Dvorak satellite intensity estimates for tropical cyclones determined from recent reconnaissance-based "best track" data. Preprints, 25th Conf. on Hurricanes and Tropical Meteorology, San Diego, CA, Amer. Meteor. Soc., 458-459.

Cintineo, R., J. A. Otkin, M. Xue, and F. Kong, 2014: Evaluating the performance of planetary boundary layer and cloud microphysical parameterization schemes in convection-permitting ensemble forecasts using synthetic GOES-13 satellite observations. *Mon. Wea. Rev.*, **142**, 163–182.

Dee, D. P., and coauthors, 2011: The ERA-Interim reanalysis: configuration and performance of the data assimilation system. *Quart. J. Roy. Meteor. Soc.,* **137**, 553-597

DiMego, G. J., and L. F. Bosart, 1982: The Transformation of Tropical Storm Agnes into an Extratropical Cyclone. Part I: The Observed Fields and Vertical Motion Computations. *Mon. Wea. Rev.*, **110**, 385–411.

Doyle, J. D., and coauthors, 2012: Real-time tropical cyclone prediction using COAMPS-TC. *Advances in Geosciences*, Vol. 28, K. Satake, Ed., World Scientific, 15-28.

Dvorak, V. F., 1984: Tropical cyclone intensity analysis using satellite data. *NOAA Tech. Report NESDIS 11*, 47 pp.

Evans, C., and R. E. Hart, 2008: Analysis of the wind field evolution associated with the extratropical transition of Bonnie (1998). *Mon. Wea. Rev.*, **136**, 2047-2065.

Evans, J. L., and R. E. Hart, 2003: Objective indicators of the life cycle evolution of extratropical transition for Atlantic tropical cyclones. *Mon. Wea. Rev.*, **131**, 909-925.

Grasso, L. D., and T. J. Greenwald, 2004: Analysis of 10.7-μm brightness temperatures of a simulated thunderstorm with two-moment microphysics. *Mon. Wea. Rev.*, **132**, 815-825.

Grasso, L. D., M. Sengupta, J. F. Dostalek, R. Brummer, and M. DeMaria, 2008: Synthetic satellite imagery for current and future environmental satellites. *Int. J. Remote Sens.*, **29**, 4373-4384.

Grasso, L., D. T. Lindsey, K.-S. S. Lim, A. Clark, D. Bikos, and S. R. Dembek, 2014: Evaluation of and suggested improvements to the WSM6 microphysics in WRF-ARW using synthetic and observed GOES-13 imagery. *Mon. Wea. Rev.*, in press.

Hart, R. E., 2003: A Cyclone Phase Space Derived from Thermal Wind and Thermal Asymmetry. *Mon. Wea. Rev.*, **131**, 585–616.

Hill, H. W., 1970: The precipitation in New Zealand associated with the cyclone of early April 1968. *N. Z. J. Sci.*, **13**, 641-662

Hong, S.-Y., Y. Noh, and J. Dudhia, 2006: A new vertical diffusion package with an explicit treatment of entrainment processes. *Mon. Wea. Rev.*, **134**, 2318–2341.

Hong, S.-Y. , and J.-O. J. Lim, 2006: The WRF single-moment 6-class microphysics scheme (WSM6). *J. Korean Meteor. Soc.,* **42,** 129 – 151

Iacono, M. J., J. S. Delamere, E. J. Mlawer, M. W. Shephard, S. A. Clough, and W. D. Collins, 2008: Radiative forcing by long-lived greenhouse gases: calculations with the AER radiative transfer models, *J. Geophys. Res.,* **113**, *D13103.*

Jankov, I., and coauthors, 2011: An evaluation of five ARW-WRF microphysics schemes using synthetic GOES imagery for an atmospheric river event affecting the California coast. *J. Hydrometeor*, **12**, 618–633.

Jarvinen, B. R., C. J. Neumann, and M. A. S. Davis, 1984: A tropical cyclone data tape for the North Atlantic basin, 1886-1983: contents, limitations, and uses. *NWS Tech. Memo. NWS NHC-22*, 21pp, NOAA, Silver Spring, Maryland.

Jimenez, P. A., J. Dudhia, J. F. Gonzalez-Rouco, J. Navarro, J. P. Montavez, and E. Garcia-Bustamante, 2012: A revised scheme for the WRF surface layer formulation. *Mon. Wea. Rev.*, **140**, 898-918.

Jin, Y., and coauthors, 2014: The impact of ice phase cloud parameterizations on tropical cyclone prediction. *Mon. Wea. Rev.*, **142**, 606–625.

Jones, S. C., and coauthors, 2003: The Extratropical Transition of Tropical Cyclones: Forecast Challenges, Current Understanding, and Future Directions. *Wea. Forecasting*, **18**, 1052–1092.

JTWC, 1995: Annual tropical cyclone report. Joint Typhoon Warning Center, Guam, 289 pp.

Karl, T. R., G. A. Meehl, and C. D. Miller, eds., 2008: *Weather and Climate Extremes in a Changing Climate: Regions of Focus: North America, Hawaii, Caribbean, and U.S. Pacific Islands*. U.S. Climate Change Science Program, 162 pp.

Klein, P. M., P. A. Harr, and R. L. Elsberry, 2000: Extratropical transition of western North Pacific tropical cyclones: an overview and conceptual model of the transformation stage. *Wea. Forecasting*, **15**, 373-395.

Kofron, D. E., E. A. Ritchie, and J. S. Tyo, 2010: Determination of a consistent time for the extratropical transition of tropical cyclones. Part II: potential vorticity metrics. *Mon. Wea. Rev.*, **138**, 4344-4361.

Lim, K.-S. S., and S.-Y. Hong, 2010: Development of an Effective Double-Moment Cloud Microphysics Scheme with Prognostic Cloud Condensation Nuclei (CCN) for Weather and Climate Models. *Mon. Wea. Rev.*, **138**, 1587–1612.

Meyers, M. P., P. J. DeMott, and W. R. Cotton, 1992: New primary ice-nucleation parameterizations in an explicit cloud model. *J. Climate Appl. Meteor.*, **31**, 708–721.

Milbrandt, J. A., and M. K. Yau, 2005: A multimoment bulk microphysics parameterization. Part II: a proposed three-moment closure and scheme description. *J. Atmos. Sci.*, **62**, 3065–3081.

Monahan A.H., J. C. Fyfe, M. H. P. Ambaum, D. B. Stephenson, and G. R. North, 2009: Empirical orthogonal function: the medium is the message. *J. Climate,* **22**, 6501 – 6514.

Morrison, H., G. Thompson, and V. Tatarskii, 2009: Impact of cloud microphysics on the development of trailing stratiform precipitation in a simulated squall line: comparison of one- and two-moment schemes. *Mon. Wea. Rev.*, **137**, 991–1007.

Olander, T., and C. Velden, 2007: The Advanced Dvorak Technique: continued development of an objective scheme to estimate tropical cyclone intensity using geostationary infrared satellite imagery. *Wea. Forecasting*, **22**, 287–298.

Olander, T. L., and C. S. Velden, 2013: ADT – Advanced Dvorak Technique Users' Guide. [Available online at http://tropic.ssec.wisc.edu/misc/adt/guides/ADTV8.1.4_Guide.pdf].

Pasch, R. J., and L. A. Avila, 1999: Atlantic hurricane season of 1996. *Mon. Wea. Rev.*, **127**, 581–610.

Rutledge, S. A., and P. V. Hobbs, 1983: The mesoscale and microscale structure and organization of clouds and precipitation in midlatitude cyclones. VIII: A model for the "seeder-feeder" process in warm-frontal rainbands. *J. Atmos. Sci.*, **40**, 1185-1206.

Schott, T., C. Landsea, G. Hafele, J. Lorens, A. Taylor, H. Thurm, B. Ward, M. Willis, and W. Zaleski, 2012: The Saffir-Simpson Hurricane Wind Scale. [Available online at http://www.nhc.noaa.gov/pdf/sshws.pdf].

Skamarock, W. C., and coauthors, 2008: A Description of the Advanced Research WRF Version 3. NCAR Technical Note NCAR/TN-475+STR, 61 pp. [Available online at http://www.mmm.ucar.edu/wrf/users/docs/arw_v3.pdf].

Stensrud, D. J., 2007: *Parameterization Schemes: Keys to Understanding Numerical Weather Prediction Models*. Cambridge University Press, 459pp.

Stewart, S. R., 2012: Tropical cyclone report: Hurricane Leslie [Available online at http://www.nhc.noaa.gov/data/tcr/AL122012_Leslie.pdf].

Thompson, G., P. R. Field, R. M. Rasmussen, and W. D. Hall, 2008: Explicit forecasts of winter precipitation using an improved bulk microphysics scheme. Part II: implementation of a new snow parameterization. *Mon. Wea. Rev.*, **136**, 5095–5115.

Van Weverberg, K., and coauthors, 2013: The Role of Cloud Microphysics Parameterization in the Simulation of Mesoscale Convective System Clouds and Precipitation in the Tropical Western Pacific. *J. Atmos. Sci.*, **70**, 1104–1128.

Velden, C., and coauthors, 2006: The Dvorak tropical cyclone intensity estimation technique: a satellite-based method that has endured for over 30 years. *Bull. Amer. Meteor. Soc.*, **87**, 1195–1210.